



UPPSALA  
UNIVERSITET

# Observations of plasma and dust around comet 67P by *Rosetta*

by

Fredrik Leffe Johansson

2019-11-26

Department of Physics and Astronomy  
Uppsala University  
SE-75120 Uppsala, Sweden

*Submitted to the Faculty of Science and Technology, Uppsala University  
in partial fulfilment of the requirements for the degree of  
Licentiate of Philosophy in Physics*





## Abstract

The instruments of the Rosetta Plasma Consortium (RPC) on the ESA mission *Rosetta* studied the comet 67P/Churyumov-Gerasimenko surroundings from August 2014 to September 2016, past perihelion and peak activity in August 2015. In this thesis, we discuss some aspects of the measurements and data from two of these instruments, the Dual Langmuir Probe instrument (RPC-LAP) and the Mutual Impedance Probe Experiment (RPC-MIP). Although a cost-effective and highly flexible plasma instrument, the simple concept of measuring current to a spherical Langmuir probe does not mean that the analysis is straight-forward. We first quantify the effect of spacecraft charging and the associated plasma sheath around the spacecraft on the in-situ measurements of RPC-LAP and RPC-MIP through numerical simulations of spacecraft-plasma interaction by use of the SPIS software package. Secondly, we study the EUV radiation intensity inside the coma by use of the photoelectron emission current obtained from LAP. We report the results of several methods (one believed to be novel) to obtain the photoemission current of RPC-LAP and use this characterise the solar EUV flux to the comet environment. We find the measured EUV flux to be significantly diminished during perihelion, and have not been able to find a credible instrumental explanation of this. Instead we present a model of attenuation of EUV by small (tens of nm) dust grains at large ( $> 2000$  km) distances from the comet, consistent with ground observations. As we do not see any local variations of EUV intensity, these small dust grains must be rare close to the nucleus, consistent with reports by in situ dust observations. This suggests that some kind of erosion process must be active as the dust grains travel outward from the cometary nucleus.

*keywords:* comets: general – spacecraft: instrumentation – plasma – Langmuir probes  
– Spacecraft-plasma interaction – dust

This licentiate thesis is based on the following papers:

### **Paper I**

**Johansson, F. L.**; Odelstad, E; Paulsson, J. J. P.; Harang, S. S. ;Eriksson, A. I., Mannel, T.; Vigren, E. ; Edberg, N. J. T. ; Miloch,W. J.; Simon Wedlund,C. ; Thiemann,E. ; Eparvier,F. ;L. Andersson. (2017)

*Rosetta photoelectron emission and solar ultraviolet flux at comet 67P*

MNRAS, **469**, S626–S635 2017, DOI: 10.1093/mnras/stx2369

### **Paper II**

**Johansson, F. L.**, Henri, P.; Eriksson, A.I.; Vallières, X., Lebreton, J-P; Béghin, C; Wattieaux, G; Odelstad, E. (2016)

*Simulations of the Rosetta Spacecraft interaction with comet plasma*

European Space Agency, Proceedings of the 14th Spacecraft Charging Technology Conference

Papers not included in this thesis:

Edberg, N. J. T.; **Johansson, F. L.**; Eriksson, A. I.; Andrews, D. J.; Hajra, R.; Henri, P.; Wedlund, C. S.; Alho, M.; Thiemann, E.

*Solar flares observed by Rosetta at comet 67P/Churyumov-Gerasimenko*

A&A A49 Volume 630, October 2019, DOI: 10.1051/0004-6361/201834834

Myllys, M.; Henri, P.; Galand, M.; Heritier, K. L.; Gilet, N.; Goldstein, R.; Eriksson, A. I. ; **Johansson, F. L.**; Deca, J.

*Plasma properties of suprathermal electrons near comet 67P/Churyumov-Gerasimenko with Rosetta*

A&A A42 Volume 630, October 2019, DOI: 10.1051/0004-6361/201834964

Breuillard, H.; Henri, P.; Bucciantini, L.; Volwerk, M.; Karlsson, T.; Eriksson, A.; **Johansson, F.**; Odelstad, E.; Richter, I.; Goetz, C.; Vallières, X.; Hajra, R.

*Properties of the singing comet waves in the 67P/Churyumov-Gerasimenko plasma environment as observed by the Rosetta mission*

A&A A39 Volume 630, October 2019, DOI: 10.1051/0004-6361/201834876

Vigren, E.; Edberg, N. J. T.; Eriksson, A. I.; Galand, M.; Henri, P.; **Johansson, F. L.**; Odelstad, E.; Rubin, M.; Vallières, X.

*The Evolution of the Electron Number Density in the Coma of Comet 67P at the Location of Rosetta from 2015 November through 2016 March*

ASJ, Volume 881, Number 1, August 2019, DOI: 10.3847/1538-4357/ab29f7

Edberg, N J; T., Eriksson, A I.; Vigren, E; **Johansson, F. L.**; Goetz, C; Nilsson, H; Gilet, N.; Henri, P.

*The Convective Electric Field Influence on the Cold Plasma and Diamagnetic Cavity of Comet 67P*

ASJ, Volume 158, Number 2, July 2019, DOI: 10.3847/1538-3881/ab2d28

Heritier, K. L.; Galand, M.; Henri, P.; **Johansson, F. L.**; Beth, A.; Eriksson, A. I.; Vallières, X.; Altwegg, K.; Burch, J. L.; Carr, C.; Ducrot, E.; Hajra, R.; Rubin, M.

*Plasma source and loss at comet 67P during the Rosetta mission*

A&A A77 Volume 618, October 2018 , DOI: 10.1051/0004-6361/201832881

Odelstad, E.; Eriksson, A. I.; **Johansson, F. L.**; Vigren, E.; Henri, P.; Gilet, N.; Heritier, K. L.; Vallières, X.; Rubin, M.; André, M.

*Ion Velocity and Electron Temperature Inside and Around the Diamagnetic Cavity of Comet 67P*

JGR Volume 123, Issue 7 July 2018 Pages 5870-5893, June 2018, DOI: 10.1029/2018JA025542

Heritier, K. L.; Altwegg, K.; Berthelier, J. -J.; Beth, A.; Carr, C. M.; De Keyser, J.; Eriksson, A. I.; Fuselier, S. A.; Galand, M.; Gombosi, T. I.; Henri, P.; **Johansson, F. L.**; Nilsson, H.; Rubin, M.; Simon Wedlund, C.; Taylor, M. G. G. T.; Vigren, E.

*On the origin of molecular oxygen in cometary comae*

Nature Communications, Volume 9, id. 2580, July 2018, DOI: 10.1038/s41467-018-04972-5

Eriksson, A. I.; Engelhardt, I. A. D.; André, M.; Boström, R.; Edberg, N. J. T.; **Johansson, F. L.**; Odelstad, E.; Vigren, E.; Wahlund, J. -E.; Henri, P.; Lebreton, J. -P.; Miloch, W. J.; Paulsson, J. J. P.; Simon Wedlund, C.; Yang, L.; Karlsson, T.; Jarvinen, R.; Broiles, T.; Mandt, K.; Carr, C. M. Galand, M.; Nilsson, H.; Norberg, C.

*Cold and warm electrons at comet 67P/Churyumov-Gerasimenko*

A&A, Volume 605, id.A15, 14 pp. September 2017, DOI: 10.1051/0004-6361/201630159

Odelstad, Elias; Stenberg-Wieser, G.; Wieser, M.; Eriksson, A. I.; Nilsson, H.; **Johansson, F. L.**

*Measurements of the electrostatic potential of Rosetta at comet 67P*

MNRAS, Volume 469, Issue Suppl\_2, S568-S581, July 2017, DOI: 10.1093/mnras/stx2232

Vigren, E.; André, M.; Edberg, N. J. T.; Engelhardt, I. A. D.; Eriksson, A. I.; Galand, M.; Goetz, C.; Henri, P.; Heritier, K.; **Johansson, F. L.**; Nilsson, H.; Odelstad, E.; Rubin, M.; Stenberg-Wieser, G.; Tzou, C. -Y.; Vallières, X.

*Effective ion speeds at  $\sim 200$ -250 km from comet 67P/Churyumov-Gerasimenko near perihelion*

MNRAS, Volume 469, Issue Suppl\_2, p.S142-S148, July 2017, DOI: 10.1093/mnras/stx1472

Heritier, K. L.; Henri, P.; Vallières, X.; Galand, M.; Odelstad, E.; Eriksson, A. I.; **Johansson, F. L.**; Altwegg, K.; Behar, E.; Beth, A.; Broiles, T. W.; Burch, J. L.; Carr, C. M.; Cupido, E.; Nilsson, H.; Rubin, M.; Vigren, E.

*Vertical structure of the near-surface expanding ionosphere of comet 67P probed by Rosetta*

MNRAS, Volume 469, Issue Suppl\_2, p.S118-S129, DOI: 10.1093/mnras/stx1459

André, M.; Odelstad, E.; Graham, D. B.; Eriksson, A. I.; Karlsson, T.; Stenberg Wieser, G.; Vigren, E.; Norgren, C.; **Johansson, F. L.**; Henri, P.; Rubin, M.; Richter, I.

*Lower hybrid waves at comet 67P/Churyumov-Gerasimenko*

MNRAS, Volume 469, Issue Suppl\_2, p.S29-S38, July 2017, DOI: 10.1093/mnras/stx868

Galand, M.; Héritier, K. L.; Odelstad, E.; Henri, P.; Broiles, T. W.; Allen, A. J.; Altwegg, K.; Beth, A.; Burch, J. L.; Carr, C. M.; Cupido, E.; Eriksson, A. I.; Glassmeier, K. -H.; **Johansson, F. L.**; Lebreton, J. -P.; Mandt, K. E.; Nilsson, H.; Richter, I.; Rubin, M.; Sagnières, L. B. M. Schwartz, S. J.; Sémon, T.; Tzou, C. -Y.; Vallières, X.; Vigren, E.; Wurz, P.

*Ionospheric plasma of comet 67P probed by Rosetta at 3 au from the Sun*

MNRAS, Volume 462, Issue Suppl\_1, p.S331-S351, November 2016, DOI: 10.1093/mnras/stw2891

Edberg, Niklas J. T.; Alho, M.; André, M.; Andrews, D. J.; Behar, E.; Burch, J. L.; Carr, C. M.; Cupido, E.; Engelhardt, I. A. D.; Eriksson, A. I.; Glassmeier, K. -H.; Goetz, C.; Goldstein, R.; Henri, P.; **Johansson, F. L.**; Koenders, C.; Mandt, K.; Möstl, C.; Nilsson, H.; Odelstad, E. Richter, I.; Wedlund, C. Simon; Stenberg Wieser, G.; Szego, K.; Vigren, E.; Volwerk, M.

*CME impact on comet 67P/Churyumov-Gerasimenko*

MNRAS, Volume 462, Issue Suppl\_1, p.S45-S56, November 2016, DOI: 10.1093/mnras/stw2112

Vigren, E.; Altwegg, K.; Edberg, N. J. T.; Eriksson, A. I.; Galand, M.; Henri, P.; **Johansson, F.**; Odelstad, E.; Tzou, C. -Y.; Vallières, X.

*Model-Observation Comparisons of Electron Number Densities in the Coma of 67P/Churyumov-Gerasimenko during January 2015*

ASJ, Volume 152, Issue 3, article id. 59, 8 pp. September 2016, DOI: 10.3847/0004-6256/152/3/59

Odelstad, E.; Eriksson, A. I.; Edberg, N. J. T.; **Johansson, F.**; Vigren, E.; André, M.; Tzou, C. -Y.; Carr, C.; Cupido, E.

*Evolution of the plasma environment of comet 67P from spacecraft potential measurements by the Rosetta Langmuir probe instrument*

GRL, Volume 42, Issue 23, pp. 10,126-10,134, December 2015, DOI: 10.1002/2015GL066599

Edberg, N. J. T.; Eriksson, A. I.; Odelstad, E.; Henri, P.; Lebreton, J. -P.; Gasc, S.; Rubin, M.; André, M.; Gill, R.; Johansson, E. P. G.; **Johansson, F.**; Vignen, E.; Wahlund, J. E.; Carr, C. M.; Cupido, E.; Glassmeier, K. -H.; Goldstein, R.; Koenders, C.; Mandt, K.; Nemeth, Z. Nilsson, H.; Richter, I.; Wieser, G. Stenberg; Szego, K.; Volwerk, M. *Spatial distribution of low-energy plasma around comet 67P/CG from Rosetta measurements* GRL Volume 42, Issue 11, pp. 4263-4269, June 2015, DOI: 10.1002/2015GL064233

*As a result of their long observations, they [the Egyptians] have prior knowledge of earthquakes and floods, of the rising of comets, and of all things which the ordinary man looks upon as beyond all finding out.*

*- Diodorus of Sicily (ca. 60-21 B.C.)*



*Till pappa*



# Contents

<b>1</b>	<b>Introduction</b>	<b>1</b>
<b>2</b>	<b>Dust and plasma around comets</b>	<b>5</b>
<b>3</b>	<b>Instruments and Methods</b>	<b>9</b>
3.1	<i>Rosetta</i> . . . . .	9
3.1.1	RPC-LAP . . . . .	12
3.1.2	RPC-MIP . . . . .	12
3.2	Langmuir Probe Data Analysis . . . . .	12
3.2.1	Electron Current . . . . .	15
3.2.2	Ion current . . . . .	15
3.2.3	Photoemission Current . . . . .	16
3.3	Simulations in SPIS . . . . .	17
<b>4</b>	<b>Reflections and Outlook</b>	<b>21</b>
<b>5</b>	<b>Summary of Publications</b>	<b>25</b>
5.1	<i>Rosetta</i> photoelectron emission and solar ultraviolet flux at comet 67P	25
5.2	Simulations of the <i>Rosetta</i> Spacecraft interaction with comet plasma .	26
<b>A</b>	<b>Paper I</b>	<b>i</b>
<b>B</b>	<b>Paper II</b>	<b>xiii</b>



# Chapter 1

## Introduction

The most striking attribute of comets must be the wonder of seeing a massive stretched feature in the night sky, like a bright gash in the black fabric of space, apparent for weeks to perhaps never reappear in a lifetime, or be a periodic but wondrous feature of the sky. Less eye-catching, but important astronomical attributes for comets are the low density and pristine icy composition of the small comet nucleus, essentially un-weathered since the dawn of its solar system. If you are more interested in what comets do instead of what they are or how they look like (actions do speak louder than words), you would be more interested in the aspect of comets as an ever-evolving obstruction in the flow of the solar wind, the medium that fills the solar system, and the intricate and multi-scale interplay comets provide. We can witness the birth and subsequent death of comet tails, atmospheres, ionospheres, bow-shocks and more as comets become more active due to their elliptical orbit as they approach the sun - to later fall dormant far from sunlight. We will discuss some of these aforementioned concepts, but for now it suffices to say that we recognise these features around planets and moons in the solar system, but we can hardly study the formation or extinction of such gigantic features anywhere else.

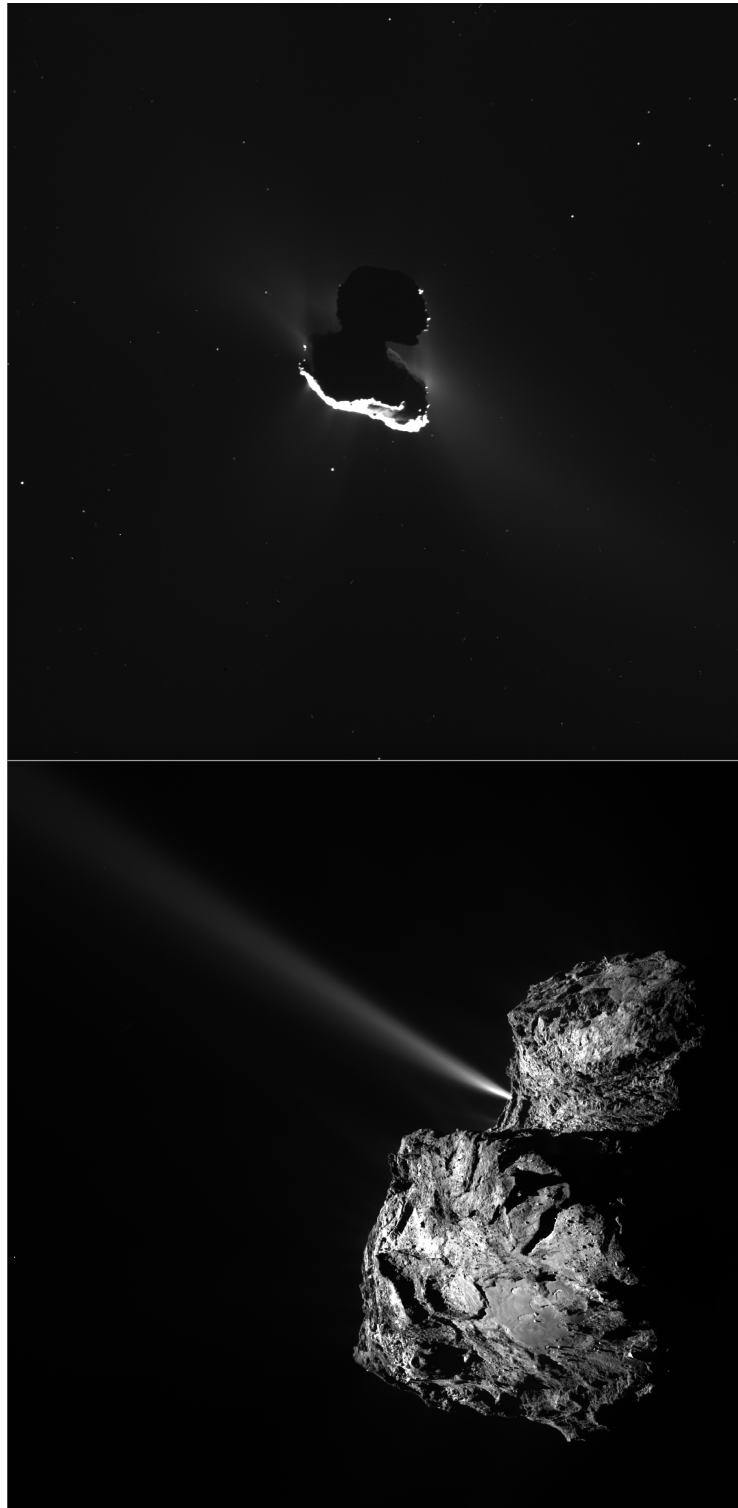


Figure 1.1: Comet 67P/Churyumov-Gerasimenko in two different illumination conditions that highlight the different expressions of cometary activity. **Top:** The comet back-lit by its own continuously emitted dusty coma, as activity is dwindling in March 2016. **Bottom:** A fully illuminated dust jet in July 2015, part of what has been dubbed the 'summer fireworks on comet 67P' (Vincent et al., 2016). Cropped and rotated images from ESA/ROSETTA/OSIRIS/NAC

Ground-based observations of comets date all the way back to 1500 B.C. with the ancient Chinese logging at least 338 apparitions (comet sightings) from 1400 B.C. to 100 A.D. (Sagan & Druyvan, 2011). Their observations were so exact and standardised that we could quantify small historic perturbations in comet 1P/Halley's orbit from present day until 240 B.C. Detailed observations of comets in the west would not start until some 3000 years later, from which Edmond Halley in 1705 concluded that three observations of comets were in fact of the same, periodic comet - then given Halley's name and (much later) earning the designation 1P for the first periodic comet. Ground-based observations have of course continued to evolve, but can still rarely resolve the nucleus by more than a pixel. The problem is not only that the nucleus is small and dark, but with improved illumination conditions closer to the sun, the dust and gas the nucleus emits will increase enough to completely obscure it from sight. Beginning in 1978, several spacecraft were launched to study comets in a series of fly-bys, with the most popular attraction being comet 1P/Halley. Due to the nature of fly-by missions, the studies were heavily constrained in observational time and proximity to the comet nuclei, but provided illuminating snapshots of cometary environments at different distances and cometary activity rates.

Extending the observation time to years and with measurements of unprecedented detail all the way down to the nucleus surface, the ESA mission *Rosetta* was launched in 2004 to rendez-vous with comet 67P/Churyumov-Gerasimenko (from here on, 67P), follow it in its orbit for several years and even place a lander on its surface. This science made possible by this mission is the main focus of this work. A general overview of the cometary mission, which ended in September 2016 is detailed in Taylor et al. (2017). The instruments that are central to this thesis are described in greater detail in Chapter 3. They allow the study of the cometary dust and plasma environment which is the topic of the next chapter, and is part of the focus of Paper I, which is discussed in Section 5.1. But to do that, we must first characterise our local spacecraft environment as explained in Sections 3.2 & 3.3, which is the topic of Paper II, discussed in Section 5.2.



## Chapter 2

# Dust and plasma around comets

The cores of comets are small. Typically cometary nuclei are only a few km in length in any direction, consisting mostly of a dark and icy substance that is loosely packed. The mass ratio of volatile ices to refractory (i.e. not so easily sublimated) materials is still a matter of debate five years after the arrival of Rosetta at 67P, but a low average mass density of about  $0.5 \text{ g/cm}^3$  could be well determined (Pätzold et al., 2016). Through interactions with other celestial objects, the otherwise inert and nearly un-processed comet can fall from its orbit in the Kuiper Belt (or possibly the Oort cloud) inwards towards the sun and become active. As the comet approaches the sun, the surface is heated and its ices sublimate to an outflowing gas, particularly in the perihelion passage, when the comet is closest in its orbit to the sun. For comet 67P, the production rate,  $Q$ , of water molecules increased three orders of magnitude from  $6 \times 10^{25} \text{ s}^{-1}$  at low activity to  $6 \times 10^{28} \text{ s}^{-1}$  at perihelion as observed by Rosetta (Hansen et al., 2016; Galand et al., 2016). These production rates are still an order of magnitude lower than what was measured at 1P/Halley (Krankowsky et al., 1986), which in turn was almost another order of magnitude below C/1995 O1 Hale-Bopp (Biver et al., 2002). This process of out-gassing generates an outward force that is capable of lifting dust (as shown in Figure 1.1) which at least at some times and locations may allow ejection of up to meter-sized boulders, as observed at 67P (Davidsson et al., 2015). Electrostatic charging can also contribute to uplift and ejection at least of small grains ( $< 50 \text{ nm}$ ) (Nordheim et al., 2015), as has been demonstrated in laboratory experiments at least for conditions relevant for the lu-

nar surface (Sickafoose et al., 2002). The gas and dust ejected fills a vast space around the comet called the comet coma. This nebulous envelope can become enormous, typically on the order of  $10^4 - 10^5$  km, and in extreme cases, larger than the sun itself (Montalto et al., 2008). Of course, the density of dust and gas drops off sharply with distance to the nucleus and both the gas and the dust are rapidly perturbed from its initial orbit by interaction with its surroundings: the radiation pressure, the gravitational pull of the sun, and the plasma emanating from the sun, the solar wind (Gombosi, 2015; Cravens, 1989).

The solar wind is a highly dynamic stream of electrons, protons and alpha particles, but tenuous even at 1 AU, about  $5 - 10 \text{ cm}^{-3}$  moving at a typical velocity of 400 km/s. For heliocentric distances  $r$  relevant for our studies, the solar wind speed does not change with  $r$  and therefore the density decreases roughly as  $1/r^2$ . Also, the solar wind carries a magnetic field that is frozen into the plasma. The neutral gas in the coma can be ionised by electron impact ionisation (Heritier et al., 2017), but will also be ionised by EUV light rays and thus create electrons and ions (Beth et al., 2019; Vigren et al., 2016) that instantly respond to and are accelerated by the electric field of the solar wind (Behar et al., 2016; Goetz et al., 2017). It is by this process observers on Earth can see two distinct cometary tails, a yellowish and relatively smooth dust tail and a blueish ion or plasma tail usually exhibiting much more fine structure. The relatively heavy dust particles are not much affected by the solar wind, though the radiation pressure of the sunlight provides some acceleration. As a result, the dust tail usually stays relatively close to the comet orbit track, though deviations can be large particularly for comets with perihelion close to the Sun. In contrast, the rapid acceleration of the ions by the solar wind electric field makes the ion tail point almost in the flow direction of the solar wind, with some aberration from the motion of the nucleus. By simple considerations of conservation of momentum, the acceleration of cometary particles will conversely slow down the solar wind in a process known as mass loading and can stagnate the flow so much as to form a bow shock (Goetz et al., 2017; Behar et al., 2017). For sufficiently high outgassing, a region called the diamagnetic cavity, into which the magnetic field cannot penetrate (Henri et al., 2017; Goetz et al., 2016), forms around the nucleus. Between the bow shock and the diamagnetic cavity we find a region often known as the magnetic pile-up region (Koenders et al., 2016), in which the magnetic field is much stronger than in the unperturbed solar wind and the plasma is dominated by cometary material. In fact, solar wind ions can be completely excluded from most of this region (Nilsson

et al., 2017; Behar et al., 2017).

Comets remain the most plausible source for dust in both the inner solar system and in the planetary debris discs of other stars (Mann, 2017). Active comets are highly effective in distributing dust to all corners of the solar system as they often arrive with highly elliptical orbits. In comparison, moons, planets and asteroids may need catastrophic events to displace and disperse mass from their gravitationally bound orbits, purely because of their own larger mass, or the mass of the planet the moon is orbiting. At comet 67P, the studied dust coming from the nucleus was dominated by  $\sim 0.1$  mm grains (Rinaldi et al., 2017) of compact particles and fluffy aggregates of submicron dust grains. Only a few single component particles have been measured in micrometer and submicrometer units (Bentley et al., 2016; Manneil et al., 2016), substantially underrepresented compared to what was extrapolated from astronomical observations by models of comet dust size distributions (Fulle et al., 2010), and in the plumes of Saturn's moon Enceladus (Hill et al., 2012). Instead, the smallest grains seem to be coming in an anti-sunward direction, with a flux that peaks at perihelion (Corte et al., 2019). The implication of this serves as a basis for the interpretation of an attenuation of UV at perihelion, detected by the Langmuir probes of Rosetta, and discussed in Paper I, Appendix A.

As background for the parametric study in Paper II, Appendix B, it is helpful to note that the gas is ionised primarily by photoionisation by EUV light rays (up to 100 nm for water molecules), or by electron impact ionisation, if the impacting electrons have comparable energies, as previously mentioned. Because the water ions are at 33,000 times heavier than the electrons, the newly emitted electrons (sometimes called photoelectrons, but hereafter referred to as "warm cometary electrons") receive almost all of the excess energy from the ionisation process, which is typically on the order of 10 eV ( $\sim 10^5$  K), and the ions are born cold, with a radial velocity profile of the neutral gas (Vigren & Galand, 2013; Cravens & Gombosi, 2004). The neutral gas also plays a role in cooling electrons by collisions, a process that is effective at high densities and outgassing rates, but infrequent for a relatively calm comet like 67P, and a mix of cold (0.1 eV) and warm (5 – 10 eV) cometary electron population is often observed (Eriksson et al., 2017; Gilet et al., 2017; Engelhardt et al., 2018).



## Chapter 3

# Instruments and Methods

### 3.1 *Rosetta*

The European space mission *Rosetta* studied the comet 67P continuously from August 2014 to September 2016 at close distance with a relative speed of order 1 m/s, from low activity at 3.8 A.U. to peak activity at the perihelion passage in the end of August 2015 (Taylor et al., 2017). In order to rendez-vous and orbit a comet for the first time, the journey through the solar system before arrival at the comet took ten years, including one gravity slingshot around Mars and three past Earth, passing the asteroids Lutetia and Steins along the way. An overview of the entire mission from launch in 2004 is shown in Figure 3.1. The *Rosetta* spacecraft measured  $2.8 \times 2.1 \times 2.0$  m, with solar arrays spanning roughly 30 m, and had a wet mass of 2.9 tonnes at launch, of which 1.6 tonnes were fuel. The spacecraft carried several instrument packages, depicted in Figure 3.2, including the lander *Philae*, to characterise the gas, dust and plasma environment and to study the nucleus surface and composition (Glassmeier et al., 2007). In this work I will highlight only two relevant instruments from the Rosetta Plasma Consortium (Carr et al., 2007).

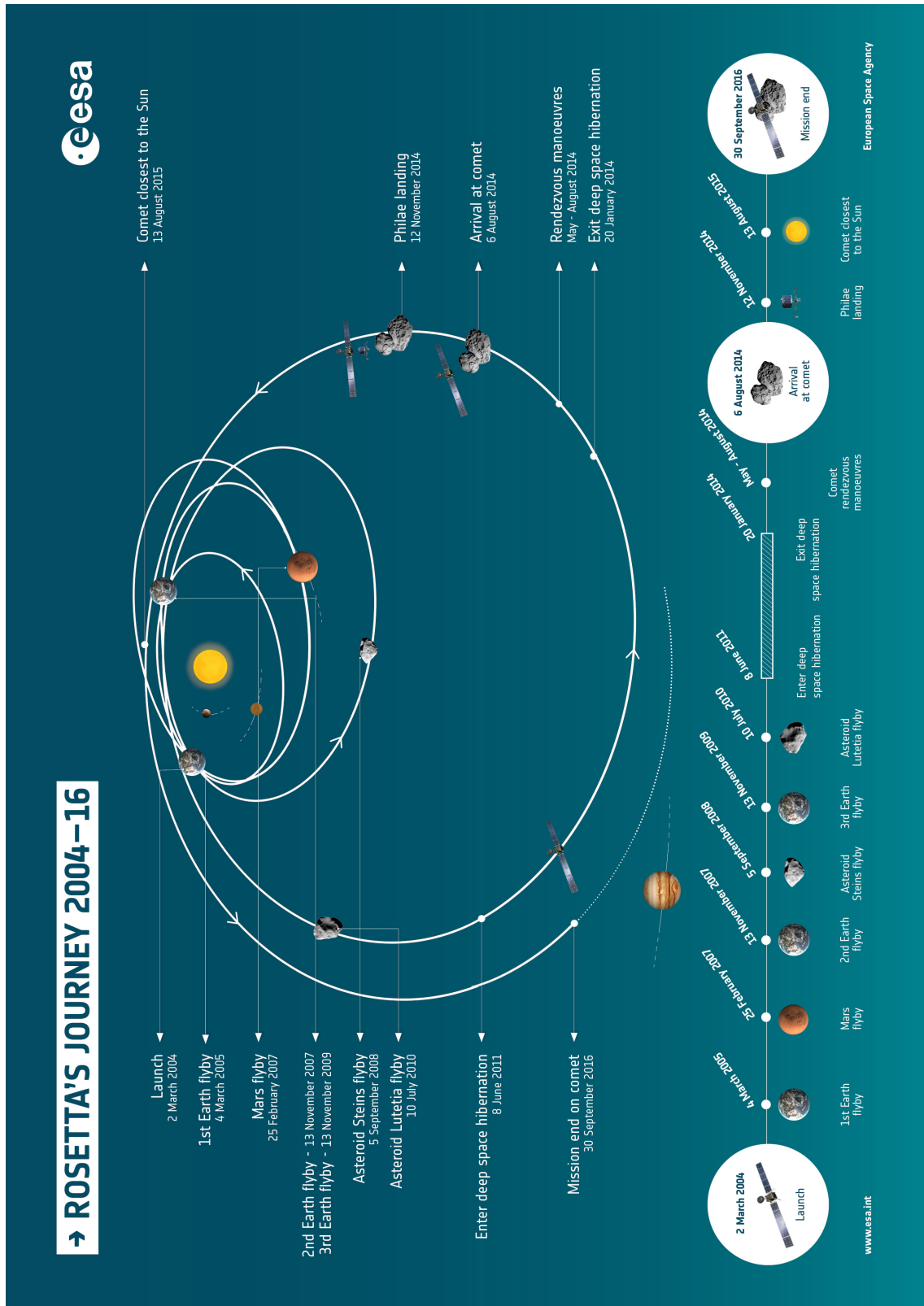


Figure 3.1: Rosetta's journey through the solar system, from the launch in 2004 to the mission end in September 2016. Image credit: ESA

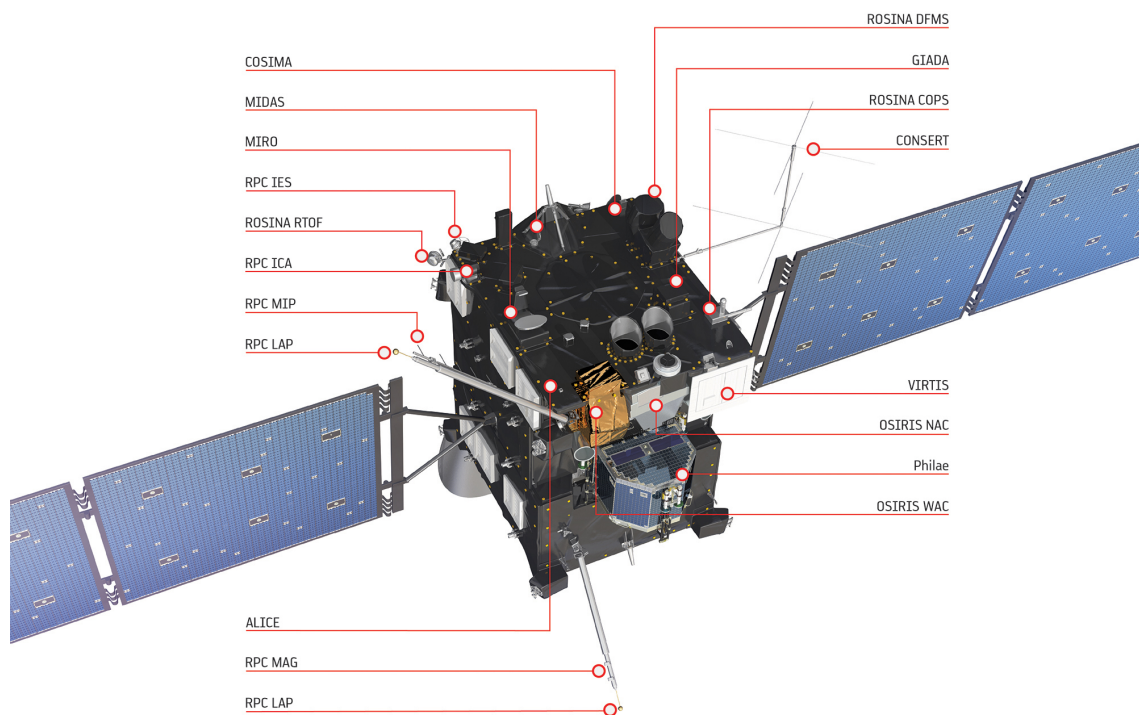


Figure 3.2: The *Rosetta* Orbiter instruments, as well as the lander Philae in stowed configuration. The upper boom in the figure carries the LAP1 probe and the MIP antenna, while LAP2 is mounted on the lower boom. Image credit: ESA/ATG medialab

### 3.1.1 RPC-LAP

The Rosetta Dual Langmuir Probe instrument (LAP) consists of two probes with Titanium Nitride coated Titanium spheres (LAP1 and LAP2) situated on two booms protruding from the spacecraft and associated electronics (Eriksson et al., 2007). The Langmuir Probes measures electric field signatures as well as the current flowing from the probe (at various potentials) to the surrounding plasma to estimate plasma parameters such as electron density, electron temperature, ion velocity, photoemission saturation current and spacecraft potential. The capabilities and particularities of LAP are discussed in conjunction with the data analysis in Section 3.2, but together with the rest of the Rosetta Plasma Consortium (RPC), for which LAP is a part of, the goal is to investigate the evolution and activity of the comet 67P plasma environment, the comet ionosphere and the interaction with the solar wind.

### 3.1.2 RPC-MIP

The Rosetta Mutual Impedance Probe experiment (MIP) consists of two transmitter/receiver antenna pairs, mounted on the LAP1 boom, and associated electronics (Trotignon et al., 2006). By driving oscillations in charge on the transmitter at a range of frequencies, it excites the surrounding plasma. Nominally, the peak signal subsequently being detected on the receiver after traversing through the plasma will then be at the plasma resonance frequency, which is proportional to the square root of the plasma (electron) density. MIP also shares operations on LAP2 situated on the LAP2 boom, so that MIP in what is known as the LDL (long Debye length) mode uses the Langmuir Probe as a transmitter to sound a greater volume and increase sensitivity for plasmas with longer Debye length, i.e. lower plasma density.

## 3.2 Langmuir Probe Data Analysis

Any body immersed in plasma, including spacecraft and Langmuir Probes, will collect charge from the incident charged particles until it reaches an equilibrium at a certain potential, which for a spacecraft is unsurprisingly called the spacecraft po-

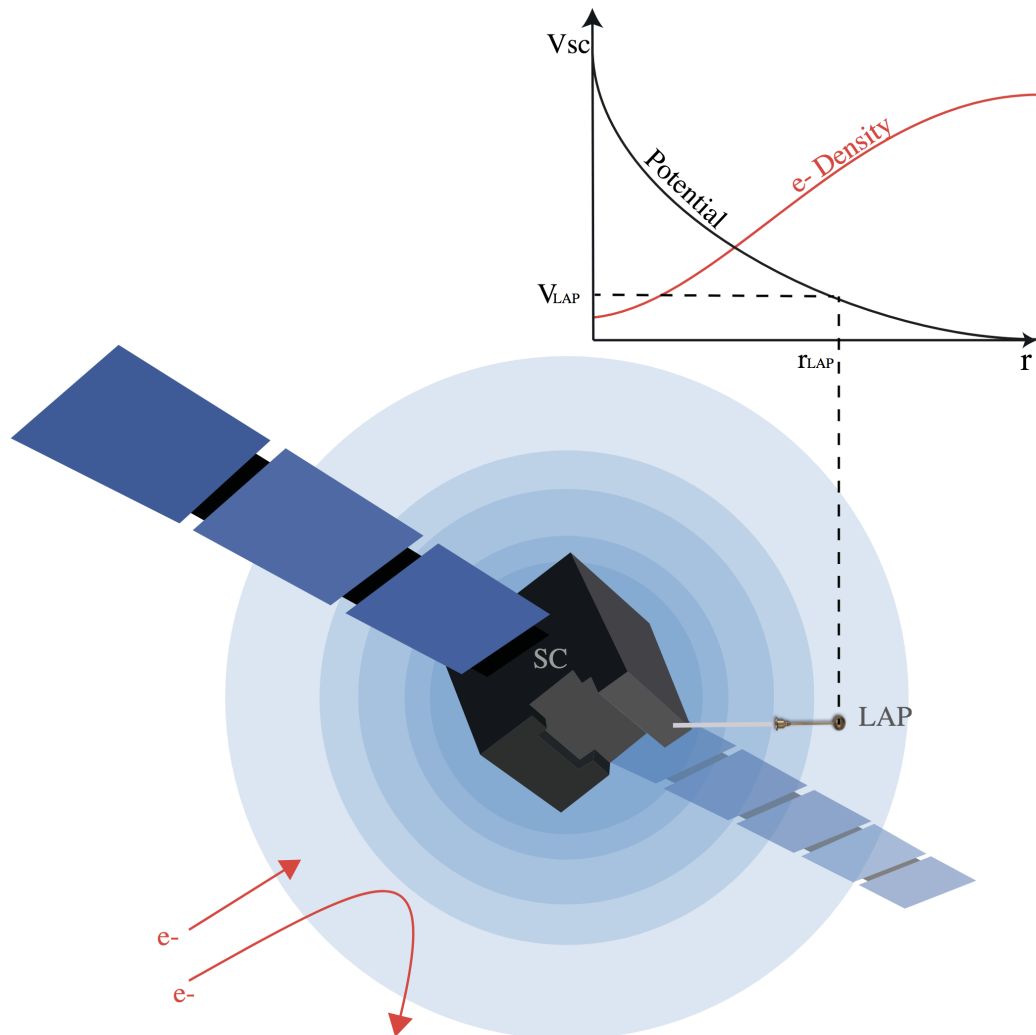


Figure 3.3: Schematic graph of the *Rosetta* spacecraft and the effect of the spacecraft potential on potential and electron density measurements at the position of the *Rosetta* Langmuir Probes. The upper boom in the Figure carries the LAP1 probe and the MIP antenna, while LAP2 is mounted on the lower boom.

tential  $V_S$ . It is helpful to separate the current to/from the probe or spacecraft into several contributions: The (plasma) electron current,  $I_e$ , the ion current  $I_i$ , and secondary currents emitted as a primary particle (or photon) interacts with the material of the probe to excite and emit electrons. In most environments, the dominating secondary current is the photoemission current  $I_{ph}$  from the photoelectric effect. There can also be various electron emission currents from particle impacts, but these can mostly be assumed to be negligible. In summary, for a spacecraft at current equilibrium,

$$I_e(V_S) + I_i(V_S) + I_{ph}(V_S) = 0. \quad (3.1)$$

In the tenuous solar wind at 1 AU,  $I_{ph}$  will typically dominate in such a way that the spacecraft will be charged to a few volts positive to re-attract the emitted photoelectrons and reduce  $I_{ph}$ . For a denser plasma around a planetary body, with electrons being more mobile than ions,  $I_e$  will typically dominate over  $I_{ph}$ , and the spacecraft will become negatively charged to repel electrons, and reduce the electron current (Odelstad et al., 2017). A schematic of this situation for Rosetta and LAP is shown in Fig 3.3.

For a more quantitative evaluation of the Langmuir Probe current, some more approximations are needed. Mott-Smith & Langmuir (1926) introduced a useful method known as Orbital-Motion-Limited theory, OML. OML assumes particle trajectories based solely on conservation of energy and angular momentum. This approach is applicable as long as the electric field from the probe does not decay too rapidly with distance, meaning the shielding effects of the plasma must not be too strong.

This can therefore be adopted when the radius of the probe  $r_p$  is smaller than the Debye length  $\lambda_D$ , which is the characteristic length scale of the Debye shielding phenomenon, the innate ability of the plasma to screen potential differences. For smaller probe radii, the describing theory is called sheath limited theory, but for the plasmas considered, we can assume  $\lambda_D > r_p$ .

### 3.2.1 Electron Current

By assuming the electron population follows a Maxwell-Boltzmann energy distribution, the current to a probe of radius  $r_p$  can be directly calculated as the flux through that volume from the random thermal motion times the charge of the electrons. For a non-drifting electron population (where thermal motion is much larger than the drift velocity), the thermal current  $I_{e0}$  to a probe at the same potential as the plasma is then

$$I_{e0} = 4\pi r_p^2 e n_e \sqrt{\frac{k_B T_e}{2\pi m_e}}, \quad (3.2)$$

where  $n_e$  is the electron density,  $T_e$  is the electron temperature and other symbols have their usual meaning.

Assuming all particles are non-magnetized and coming from a zero potential at infinity, by energy and angular momentum conservation considerations from OML it can be shown (Mott-Smith & Langmuir, 1926) that the electron current  $I_e$  to a spherical probe is

$$I_e = \begin{cases} I_{e0} \left(1 + \frac{eV_p}{k_B T_e}\right) & \text{for } V_p \geq 0 \\ I_{e0} \exp\left(\frac{eV_p}{k_B T_e}\right) & \text{for } V_p < 0, \end{cases} \quad (3.3)$$

where  $V_p$  is the absolute potential of the probe. The Langmuir probe can be biased to some potential  $V_b$  from the spacecraft potential  $V_S$  according to

$$V_p = V_b + V_S, \quad (3.4)$$

making it possible to compare measured current to the expressions in Eq 3.3.

### 3.2.2 Ion current

As ions are heavier than electrons, their thermal speed is much lower than that of the electrons even if their temperatures are equal. In the plasmas of interest to us, the electron temperature is usually much higher than  $T_i$ , further emphasising this

difference. The ion flow is often supersonic, so that we can simplify the ion current  $I_{i0}$  to the probe when at the potential of the plasma by

$$I_{i0} = \pi r_p^2 q_i n_i u_i, \quad (3.5)$$

where  $q_i$  is the ion charge,  $n_i$  is the ion density and  $u_i$  is the effective velocity of the ions. It can be shown (Fahleson et al., 1974) that the ion current  $I_i$  to a probe at a general potential is then

$$I_i = \begin{cases} -I_{i0} \left(1 - \frac{eV_p}{E_i}\right) & \text{for } V_p < E_i/e \\ 0 & \text{for } V_p > E_i/e, \end{cases} \quad (3.6)$$

where  $E_i$  is the kinetic energy  $\frac{1}{2}m_i u_i^2$  of ions of mass  $m_i$ . We use the usual sign convention of considering currents as positive when flowing from the probe to the plasma.

### 3.2.3 Photoemission Current

As discussed in the beginning of the section, the probe and the spacecraft body will emit photoelectrons as they are subjected to sunlight. The magnitude of this current depends on material properties, the incident EUV flux and the potential of the object, as for positive potentials some photoelectrons can be re-attracted and reabsorbed, so that they carry no net current to or from the probe. However, it is the electric field of the plasma immediately surrounding the probe that determines the net force acting on the newly emitted electron, such that at some potential  $V_{\dagger} = 0$  we shift from net repulsion to attraction. For a probe inside the electrostatic potential field of another body such as a spacecraft as sketched in Fig 3.3, if the absolute potential at the probe position ( $V_{LAP}$  in the same figure) is some factor  $\alpha$  of the spacecraft potential, we can define

$$V_{\dagger} = V_b + \alpha V_S, \quad (3.7)$$

in analogy to Eq 3.4.

Grard (1973) describes the case of a Maxwell-Boltzmann distribution of electrons emitted isotropically from a photoemitting probe and shows that the photoemission

current  $I_{\text{ph}}$  from a sphere becomes

$$I_{\text{ph}} = \begin{cases} -I_{\text{ph}0} \exp\left(\frac{-eV_{\dagger}}{k_{\text{B}}T_{\text{ph}}}\right) & \text{for } V_{\dagger} \geq 0 \\ -I_{\text{ph}0} & \text{for } V_{\dagger} < 0, \end{cases} \quad (3.8)$$

where  $T_{\text{ph}}$  is the maxwellian temperature of the emitted photoelectrons,  $I_{\text{ph}0}$  is the photosaturation current of the probe surface, and we have modified the equation to accommodate the definition of  $V_{\dagger}$ .

Taking all of this together, an example of each current contribution to the total current with varying voltage (a voltage sweep) in a plasma is sketched in Figure 3.4, where  $V_{\dagger} = 0$  is indicated by  $V_{\text{ph}}$  in the figure. An accurate identification of  $I_{\text{ph}0}$  and  $V_{\text{ph}}$  is needed to accurately estimate the ion and electron characteristics, and is the focus of Paper I in Appendix A. As the photoemission current is due to the solar EUV radiation it serves as a measure of the intensity of this radiation. There is no other such measurement on Rosetta, so it is of high scientific interest to evaluate the LAP measurements of photoelectron emission throughout the mission. We have done so in Paper I, by several methods of analysing the data, finding a significant decrease of EUV intensity at high comet activity despite what should be an optically thin gas atmosphere at these wavelengths.

### 3.3 Simulations in SPIS

The Spacecraft-Plasma Interaction System (SPIS) ([Matéo-Vélez et al., 2012](#); [SPINE, 2013](#); [Thiébaud, 2012](#)) is a software package developed mainly by ONERA/Artemum on an ESA contract. Essentially it is an electrostatic PIC or hybrid solver. Electromagnetic effects are not considered, and the electrostatic potential is found by solving Gauss's law for the electric field. Plasma populations can e.g. be simulated as particles or be assumed to be in Boltzmann equilibrium at given temperature with the potential. The latter approximation works well for repelling potentials, i.e. for space around negatively charged objects. Plasma particle distributions can be specified as superpositions of several stationary or flowing Maxwellians at various temperatures, and secondary emission is included by realistic models, with an extensive database of relevant material properties. The purpose is not only to investigate the spacecraft

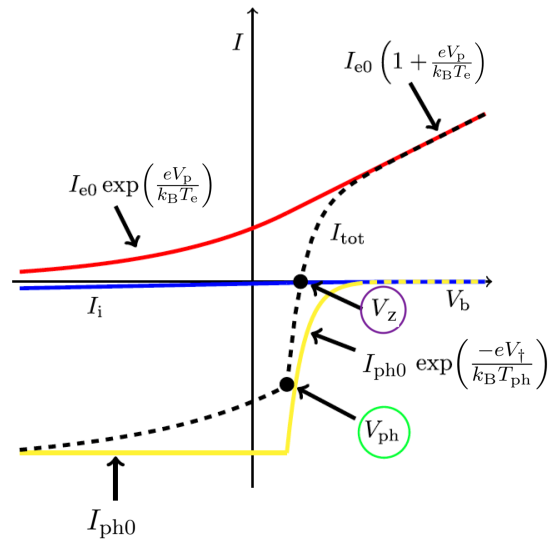


Figure 3.4: Langmuir Probe bias voltage sweep sketch, with contributions to the total probe current  $I_{\text{tot}}$  (dashed) from photoelectron emission (yellow), plasma ions (blue) and plasma electrons (red). Here  $I_{e0}$  and  $I_{i0}$  are proportional to the density and characteristic speeds of electrons and ions, respectively, while  $I_{\text{ph}0}$  depends on the solar EUV intensity and material properties of the probe. Two  $V_S$  estimates  $V_z$  and  $V_{\text{ph}}$ , are highlighted by magenta and green circles, respectively. Figure adapted with permission from the author (Odelstad, 2018).

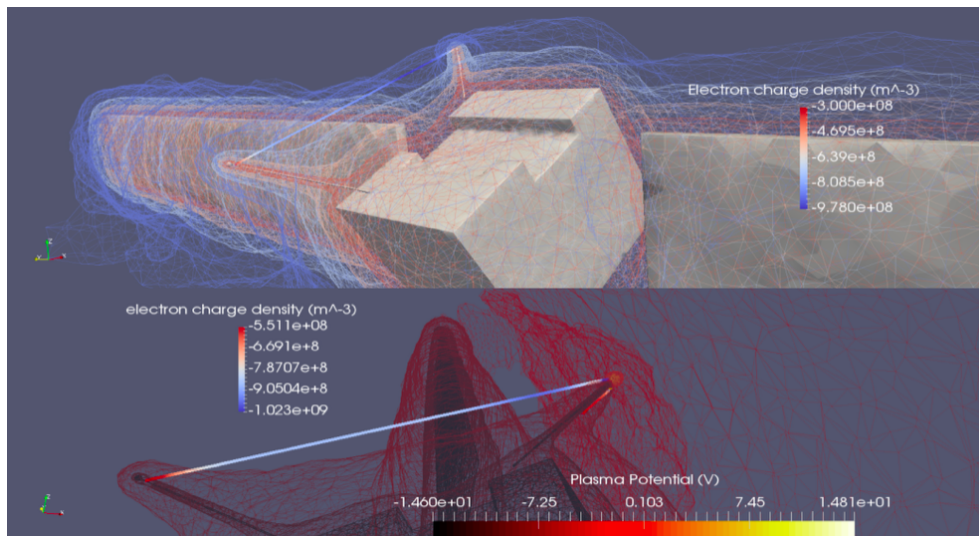


Figure 3.5: **Top**: Plasma electron density iso-surfaces (increasing density from blue to red) from a SPIS simulation, showing how a spacecraft charged to  $-14.6$  V repels electrons (simulated as a Maxwell-Boltzmann distribution with temperature  $T_e = 5$  eV) and reduces the electron density around the spacecraft. Also picturing a line of sight density profile from the two probes **Bottom**: Equipotential shells (white to black, through red) of the same SPIS simulation. Also note that one of the two Langmuir probes on is charged  $+15.4$  V, and the other is at the same potential as the spacecraft. Figure adapted from [Johansson et al. \(2016\)](#)

charging (internal and surface charging) of the materials on a spacecraft in various environments, but also to investigate the effect that has on in-situ measurements on scientific instruments such as the Langmuir Probe and particle detectors. Simulation output ranges from 3-D electrostatic potential and density maps (as shown in Figure 3.5) and simulated Langmuir probe sweeps or particle detector counts.

SPIS includes special provisions for simulation of Langmuir probes and plasma particle instruments by means of back-tracking ([Sarrailh et al., 2015](#)). This is an efficient test particle method of getting good statistics on particle fluxes hitting a small detector area without an excessive total number of simulation particles. Particles are emitted from the probe and tracked through the fields found by the Poisson solver to whatever boundary they end up on, and the current is then weighted by the value of the distribution function on the boundary ([Cully et al., 2007](#)). Obviously back-tracked particles are always considered as particles in such a simulation, even when

the plasma solver itself uses Boltzmann electrons. It is therefore possible to simulate also the current to positive spacecraft elements with little error as long as these elements are small (like a Langmuir probe) compared to the spacecraft size and the Debye length as in the example in Figure 3.5. In Paper II in Appendix B we used SPIS simulations to investigate local perturbations of the plasma near the MIP and LAP sensors. We found significant such changes, which among else should result in that the plasma density from the MIP instrument should depend on what mode it is operated in. As discussed in Section 5.2, this effect was not observed, inspiring different investigations of the MIP measurement principle by [Wattiaux et al. \(2019\)](#) which indeed showed that this can be explained by MIP actually not measuring the local plasma around the antenna.

## Chapter 4

# Reflections and Outlook

The photoemission study (Paper I) showed an unexpected decrease of photoelectron emission with increasing comet activity. We showed that this can be explained by the presence of small (tens of nm) dust grains at large distance ( $\gtrsim 2000$  km) from the nucleus, but that these small grains cannot be produced directly by the nucleus as we then would have been able to find variations of the attenuation with the cometocentric distance of Rosetta. The presence of small grains at large distance is consistent with ground observations (Boehnhardt et al., 2016) and their absence close to the comet with in situ dust observations on Rosetta (Rinaldi et al., 2017; Mannel et al., 2019; Corte et al., 2019). In this way, our results indicate how these apparently disparate results can be reconciled. Such a reconciliation would imply dust fragmentation or erosion, a process much discussed (Mann, 2017; Boehnhardt et al., 2016). The dynamics of dust in space is of course of high interest for many processes, including the formation and evolution of planetary systems. Planetary formation studies mainly consider the agglomeration of smaller grains to larger (and ultimately to macroscopic bodies like comet nuclei and planets), but in this context it is also of interest to estimate the importance of processes in the other direction, toward smaller grains. We cannot claim to have results immediately useful in this context, but if the interpretation we propose survive further investigations and is extended by better quantitative modelling, it may in the end contribute to a better understanding of fragmentation/erosion processes of cosmic dust grains.

The spacecraft-plasma simulations presented in Paper II have been continued, particularly regarding the impact on LAP ion measurements. Low energy ions are very hard to measure with the body-mounted RPC-ICA and RPC-IES instruments on Rosetta as the spacecraft potential is usually very negative, so that the ions are accelerated toward the spacecraft and much information on their flow is lost (Bergman et al., 2019). The LAP ion current is therefore an important source of information on the low energy (few eV) ions (Odelstad et al., 2018) which must be understood to determine the reliability of the information obtained. We will therefore continue these simulations and present them in forthcoming papers. However, also the spacecraft potential needs to be better understood. As shown by Odelstad et al. (2015) and Odelstad et al. (2017), the Rosetta spacecraft was negatively charged during most of the main mission at comet 67P. This was interpreted as a natural effect of warm cometary electrons, e.g. electrons recently released by photoionisation of the cometary gas. Such electrons have a broad energy distribution with typical energies of a few tens of eV (Vigren & Galand, 2013), so when their flux overcomes the spacecraft photoelectron emission and the flux of collected ions, the spacecraft should indeed charge negatively. Since electrons typically have much higher velocity than the heavier positive ions, a freely floating conductor in a plasma typically charges to a negative voltage of magnitude a few times the characteristic energy of the electrons, so the observed negative potentials (typically -15 V) qualitatively agree well with the presence of warm (5-10 eV) cometary electrons. A puzzling detail is that the spacecraft potential appears to be very negative also for events when most of the plasma electrons are much colder. Eriksson et al. (2017) showed that the LAP data often shows characteristics of two electron populations, the warm electrons and a much colder distribution at 0.1 eV (1000 K) or less. This can readily be interpreted as the co-existence of recently released cometary electrons and similar electrons which have had the time to cool by collisional interaction with the cold (about 300 K) cometary gas. The co-existence of these populations was verified by completely independent means by Gilet et al. (2017). Engelhardt et al. (2018) showed that the cold electrons were seen over a large fraction of the main Rosetta mission, preferentially at times when a simple model indicate electron cooling should be most efficient. Because of the consistently negative spacecraft potential, it was assumed that the warm cometary electrons still dominate the flux in these events. Recently, Gilet et al. (2019) verified and extended these statistics, including a verification of the presence of both populations.

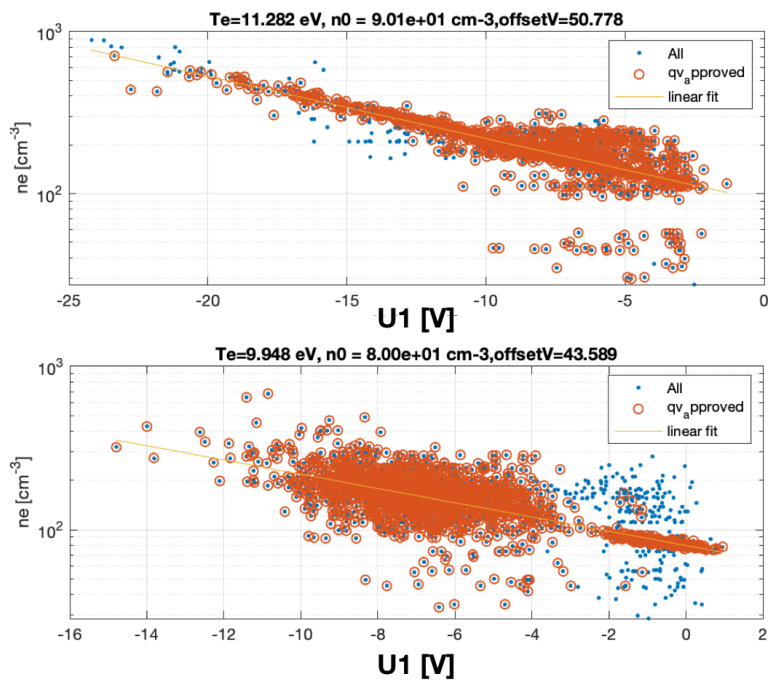


Figure 4.1: Measured electron density (log) by MIP vs simultaneously measured spacecraft potential by LAP for two short consecutive periods **Top**: 2015-09-24 to 2015-09-26 **Bottom**: 2015-09-27 (all day). The physical interpretation of the slope yields an effective electron temperature of around  $\sim 10$  eV.

All this seems qualitatively consistent, but there may still be unknown effects hiding. In the cross-calibration of the LAP and MIP datasets, we have found a very good correlation between total plasma density (as determined by MIP) and spacecraft potential (measured by LAP), as seen in Figure 4.1. As the cold electrons should hardly contribute any flux at all to the spacecraft, one would expect that what should really correlate to the spacecraft potential is the warm electron density. We have not yet been able to investigate if this is the case, but given the strong correlation of total electron density to spacecraft potential, it would seem this could only be the case if the fraction of cold electrons is relatively constant, or at least increasing smoothly and not too drastically with density. The very variable values of this ratio found by [Gilet et al. \(2019\)](#) suggests this may not be the case. If so, one is left to explain why total electron density should matter. An interesting possibility would be the influence of exposed positively biased elements on the solar panels, like the bus bars terminating solar cell strings. This possibility remains to investigate and model, and of course the data should be analysed for finding evidence for or against such an effect. A good experimental test would be to investigate the correlation of spacecraft potential to the warm plasma density as determined in [Gilet et al. \(2019\)](#). If a better correlation is found than to the total plasma density, there should be little reason to worry, but in the opposite case a simulation model including the influence of the solar panels may have to be considered.

## Chapter 5

# Summary of Publications

### 5.1 *Rosetta* photoelectron emission and solar ultraviolet flux at comet 67P

When characterising the photoemission current on the Langmuir Probes, we find that the photoemission indicates an unexpected attenuation of the EUV flux that mirrors the cometary activity. Several hypotheses for this attenuation are given, all discarded except one: the attenuation following erosion or fragmentation of dust grains down to nanometer scales (20 nm radius) far (>2000 km) from the comet nucleus. Dust particles at these sizes have suspiciously been missing from in-situ *Rosetta* measurements of dust flowing from the comet, and our result is another piece of a growing body of evidence suggesting that the main production of cometary nanodust is far from the source (the comet surface). The dust model notwithstanding, the attenuation of EUV also has an impact of photoionisation of cometary gas, and may play a role in why current cometary plasma production models does not agree well with *Rosetta* measurements of plasma at perihelion. We also report in detail on three different methods for estimating the photoemission from a Langmuir probe, one of them believed to be new.

## 5.2 Simulations of the *Rosetta* Spacecraft interaction with comet plasma

We simulate the plasma-spacecraft interaction in a parametric study of 17 environments with parameters typical of cometary plasma to quantify spacecraft charging influence on RPC measurements. The 3-D potential and plasma density map can be and was exported to further simulate a MIP sounding experiment in a realistic volume, and served as a guide for operations of both MIP and LAP (the majority of the simulations were completed under 2015). The results, although not surprising, quantified the electron density depletion around the instruments, consistent with LAP sweep analysis, and suggest that MIP measurements in LDL mode should be significantly less disturbed by the electron density depletion than in other modes. However, it has later been shown that consecutive measurements of MIP in or outside of LDL mode are consistent even when the spacecraft charging is significant, it suggests that MIP is less disturbed by the spacecraft potential than expected. Which suggests that there must be some effect making the MIP measurement much less local than then the LAP observations, so that MIP effectively excites the plasma frequency in a large volume surrounding the spacecraft. A further indication of this is that the plasma density determined from MIP is much smoother than that indicated by LAP ion or electron current, as expected for a volume average on scales much larger than the antenna. If the MIP instrument can be described as not only oscillating a charge ( $+q$ ) on the transceivers, but also a mirror charge ( $-q$ ) on the spacecraft ground that is carried to the entire (conductive and electronically connected) solar array, in effect increasing the baseline to an antenna of 32 m, then the MIP detected plasma frequency would be from an excitation of the plasma frequency of a much larger volume, and be less sensitive to disturbances and screening. This hypothesis is also in-line with why the signal-to-noise ratio is notably better when the two MIP transmitters are working in phase (oscillating  $-2q$  on spacecraft ground) than in anti-phase ( $\approx 0 q$  on spacecraft ground). A recent detailed study by [Wattiaux et al. \(2019\)](#) confirms this reasoning, with a lot more details and a much better numerical understanding. Why our results in Paper II differed from MIP observations can therefore now be considered explained.

# Acknowledgements

I don't believe anyone got where they are without help.

I want to thank everyone that has ever helped me over the years. From surviving in Frankfurt (and Orléans!) without money or ID, to offering me a place to stay, a train ticket out of the country, a car-ride, **the best job ever**, a favour, a beer, some food, a hug, a hand, an ear, a cup of coffee, **friendship**, feedback, collaboration, encouragement, advice and **a home**.

You know who you are, and I'm forever trying to pay you all back.

Or pay it forward.

.

.

Och Anders...

Tack!



# Bibliography

- Behar, E., Lindkvist, J., Nilsson, H., et al. 2016, *Astronomy & Astrophysics*, 596, A42
- Behar, E., Nilsson, H., Alho, M., Goetz, C., & Tsurutani, B. 2017, *Monthly Notices of the Royal Astronomical Society*, 469, S396
- Bentley, M. S., Arends, H., Butler, B., et al. 2016, *Acta Astronautica*,
- Bergman, S., Stenberg Wieser, G., Wieser, M., Johansson, F. L., & Eriksson, A. 2019, *Journal of Geophysical Research: Space Physics*, under review
- Beth, A., Galand, M., & Heritier, K. L. 2019, *Astronomy & Astrophysics*, 630, A47
- Biver, N., Bockelée-Morvan, D., Colom, P., et al. 2002, *Earth, Moon, and Planets*, 90, 5
- Boehnhardt, H., Riffeser, A., Kluge, M., et al. 2016, *Monthly Notices of the Royal Astronomical Society*, 462, S376
- Carr, C., Cupido, E., Lee, C. G. Y., et al. 2007, *Space Sci. Rev.*, 128, 629
- Corte, V., Rotundi, A., Zakharov, V., et al. 2019, *Astronomy & Astrophysics*, 630
- Cravens, T. E. 1989, *Advances in Space Research*, 9, 293
- Cravens, T. E. & Gombosi, T. I. 2004, *Advances in Space Research*, 33, 1968
- Cully, C., Ergun, R. E., & Eriksson, A. I. 2007, *J. Geophys. Res.*, 112, A09211, doi:10.1029/2007JA012269
- Davidsson, B. J. R., P. J. Gutierrez, H. Sierks, et al. 2015, *Astronomy & Astrophysics*
- Engelhardt, I. A. D., Eriksson, A. I., Vigren, E., et al. 2018, *A&A*, 616, A51

- Eriksson, A. I., Boström, R., Gill, R., et al. 2007, *Space Sci. Rev.*, 128, 729
- Eriksson, A. I., Engelhardt, I. A. D., André, M., et al. 2017, *Astronomy & Astrophysics*
- Fahleson, U., Fälthammar, C.-G., & Pedersen, A. 1974, *Planetary and Space Science*, 22, 41
- Fulle, M., Colangeli, L., Agarwal, J., et al. 2010, *Astron. Astrophys.*, 522, A63
- Galand, M., Héritier, K. L., Odelstad, E., et al. 2016, *Monthly Notices of the Royal Astronomical Society*, 462, S331
- Gilet, N., Henri, P., Wattieaux, G., Cilibrasi, M., & Béghin, C. 2017, *Radio Science*, 52, 1432
- Gilet, N., Henri, P., Wattieaux, G., et al. 2019, *Frontiers in Astronomy and Space Sciences*, 6, 16
- Glassmeier, K.-H., Boehnhardt, H., Koschny, D., Kührt, E., & Richter, I. 2007, *Space Sci. Rev.*, 128, 1
- Goetz, C., Koenders, C., Richter, I., et al. 2016, *Astronomy & Astrophysics*, 588, A24
- Goetz, C., Volwerk, M., Richter, I., & Glassmeier, K.-H. 2017, *Monthly Notices of the Royal Astronomical Society*, 469, S268
- Gombosi, T. I. 2015, in *Magnetotails in the Solar System* (John Wiley and Sons, Inc), 169–188
- Grard, R. J. L. 1973, *Journal of Geophysical Research*, 78, 2885
- Hansen, K. C., Altwegg, K., Berthelier, J.-J., et al. 2016, *Monthly Notices of the Royal Astronomical Society*, 462, S491
- Henri, P., Vallières, X., Hajra, R., et al. 2017, *Monthly Notices of the Royal Astronomical Society*, 469, S372
- Héritier, K. L., Altwegg, K., Balsiger, H., et al. 2017, *Monthly Notices of the Royal Astronomical Society*, 469, S427
- Hill, T. W., Thomsen, M. F., Tokar, R. L., et al. 2012, *J. Geophys. Res.*, 117, A05209
- Johansson, F. L., Henri, P., Eriksson, A., et al. 2016, in *Proceedings of the 14th Spacecraft Charging Technology Conference* (European Space Agency)

- Koenders, C., Goetz, C., Richter, I., Motschmann, U., & Glassmeier, K.-H. 2016, *Monthly Notices of the Royal Astronomical Society*
- Krankowsky, D., Lämmerzahl, P., Herrwerth, I., et al. 1986, *Nature*, 321, 326
- Mann, I. 2017, *Philosophical Transactions of the Royal Society of London A: Mathematical, Physical and Engineering Sciences*, 375
- Mannel, T., Bentley, M. S., Boakes, P. D., et al. 2019, *A&A*, 630, A26
- Mannel, T., Bentley, M. S., Schmied, R., et al. 2016, *Monthly Notices of the Royal Astronomical Society*, 462, S304
- Matéo-Vélez, J.-C., Sarrailh, P., Thiébault, B., et al. 2012, in *Proceedings of the 12th Spacecraft Charging Technology Conference (SCTC-12) (JAXA)*
- Montalto, M., Riffeser, A., Hopp, U., Wilke, S., & Carraro, G. 2008, *A&A*, 479, L45
- Mott-Smith, H. M. & Langmuir, I. 1926, *Physical review*, 28, 727
- Nilsson, H., Wieser, G. S., Behar, E., et al. 2017, 469, S252
- Nordheim, T. A., Jones, G. H., Halekas, J. S., Roussos, E., & Coates, A. J. 2015, *Planetary and Space Science*,
- Odelstad, E. 2018, Licentiate thesis, Uppsala University, Swedish Institute of Space Physics, Uppsala, Rosetta spacecraft potential and activity evolution of comet 67P
- Odelstad, E., Eriksson, A. I., Edberg, N. J. T., et al. 2015, *Geophys. Res. Lett.*, 42, 10,126
- Odelstad, E., Eriksson, A. I., Johansson, F. L., et al. 2018, *Journal of Geophysical Research (Space Physics)*, 123, 5870
- Odelstad, E., Stenberg-Wieser, G., Wieser, M., et al. 2017, *Monthly Notices of the Royal Astronomical Society*, 469, S568
- Pätzold, M., Andert, T., Hahn, M., et al. 2016, *Nature*, 530, 63
- Rinaldi, G., Della Corte, V., Fulle, M., et al. 2017, *Monthly Notices of the Royal Astronomical Society*, 469, S598
- Sagan, C. & Druyan, A. 2011, *Comet* (Random House Publishing Group), google-Books-ID: LhkoowKFtTsC

- Sarrailh, P., Matéo-Vélez, J.-C., Hess, S. L., et al. 2015, *IEEE Transactions on Plasma Science*, 43, 2789
- Sickafoose, A. A., Colwell, J. E., Horányi, M., & Robertson, S. 2002, *Journal of Geophysical Research: Space Physics*, 107, SMP 37
- SPINE. 2013, SPINE community Web site
- Taylor, M. G. G. T., Altobelli, N., Buratti, B. J., & Choukroun, M. 2017, *Philosophical Transactions of the Royal Society of London A: Mathematical, Physical and Engineering Sciences*, 375
- Thiébaud, B. 2012, *SPIS-GEO User Manual*, esa-spisgeo-d7-sum-2012-08-002 edn. (Paris: Artenum)
- Trotignon, J. G., Michau, J. L., Lagoutte, D., et al. 2006, *Space Science Reviews*, 128, 713
- Vigren, E., Altwegg, K., Edberg, N. J. T., et al. 2016, *The Astronomical Journal*, 152, 59
- Vigren, E. & Galand, M. 2013, *Ap. J.*, 772, 33
- Vincent, J.-B., A'Hearn, M. F., Lin, Z.-Y., et al. 2016, *Monthly Notices of the Royal Astronomical Society*, 462, S184
- Wattieaux, G., Gilet, N., Henri, P., Vallières, X., & Bucciantini, L. 2019, *A&A*, 630, A41

# Appendix A

## Paper I



# *Rosetta* photoelectron emission and solar ultraviolet flux at comet 67P

Fredrik L. Johansson,<sup>1,2★</sup> E. Odelstad,<sup>1,2</sup> J. J. P. Paulsson,<sup>3</sup> S. S. Harang,<sup>3</sup>  
A. I. Eriksson,<sup>1</sup> T. Mannel,<sup>4,5</sup> E. Vigren,<sup>1</sup> N. J. T. Edberg,<sup>1</sup> W. J. Miloch,<sup>3</sup>  
C. Simon Wedlund,<sup>3</sup> E. Thiemann,<sup>6</sup> F. Eparvier<sup>6</sup> and L. Andersson<sup>6</sup>

<sup>1</sup>Swedish Institute of Space Physics, Box 537, SE-75121 Uppsala, Sweden

<sup>2</sup>Department of Physics and Astronomy, Uppsala University, Box 516, SE-75120 Uppsala, Sweden

<sup>3</sup>Department of Physics, University of Oslo, Sem Sælands vei 24, Postbox 1048, 0317 Oslo, Norway

<sup>4</sup>Space Research Institute, Austrian Academy of Sciences, Schmiedlstrasse 6, A-8042 Graz, Austria

<sup>5</sup>Physics Institute, University of Graz, Universitätsplatz 5, A-8010 Graz, Austria

<sup>6</sup>Laboratory for Atmospheric and Space Physics, University of Colorado, 3665 Discovery Drive Boulder, CO 80303, USA

Accepted 2017 September 10. Received 2017 September 6; in original form 2017 April 12

## ABSTRACT

The Langmuir Probe instrument on *Rosetta* monitored the photoelectron emission current of the probes during the *Rosetta* mission at comet 67P/Churyumov-Gerasimenko, in essence acting as a photodiode monitoring the solar ultraviolet radiation at wavelengths below 250 nm. We have used three methods of extracting the photoelectron saturation current from the Langmuir probe measurements. The resulting data set can be used as an index of the solar far and extreme ultraviolet at the *Rosetta* spacecraft position, including flares, in wavelengths which are important for photoionization of the cometary neutral gas. Comparing the photoemission current to data measurements by MAVEN/EUVM and TIMED/SEE, we find good correlation when 67P was at large heliocentric distances early and late in the mission, but up to 50 per cent decrease of the expected photoelectron current at perihelion. We discuss possible reasons for the photoemission decrease, including scattering and absorption by nanograins created by disintegration of cometary dust far away from the nucleus.

**Key words:** plasmas – methods: data analysis – Sun: UV radiation – comets: individual: 67P/Churyumov-Gerasimenko – dust, extinction.

## 1 INTRODUCTION

ESA's comet-chaser *Rosetta* arrived at comet 67P/Churyumov-Gerasimenko in 2014 August and completed its mission in 2016 September. During all this time, the instruments of the Rosetta Plasma Consortium (RPC) were monitoring the plasma environment. The Langmuir probe instrument (RPC-LAP), described in detail by Eriksson et al. (2007), measures the current between the probe and surrounding space with the aim to characterize the plasma. When the probes are sunlit, they also measure the current due to excitation and emission of electrons from light, as discovered by Hertz (1887) and famously interpreted by Einstein (1905). The photoemission saturation current of a Langmuir probe depends on the solar far and extreme ultraviolet spectrum, and has successfully been used as a proxy for the solar UV flux on previous studies around Venus (Brace, Hoegy & Theis 1988; Hoegy et al. 1993). For plasma science, the UV flux has implications on spacecraft charging, as well as a fundamental source for plasma from the ionization

of neutrals around e.g. a comet (Vigren & Galand 2013; Bodewits et al. 2016; Galand et al. 2016; Vigren et al. 2016). The photoemission, like the solar flux, should follow an  $r^{-2}$  relation as *Rosetta* approaches and retreats from comet perihelion.

We compare the photoemission observed by RPC-LAP from 2014 May to the end of mission in 2016 September to the expected photoemission using UV observations from the SEE experiment (Woods et al. 2005) on the TIMED spacecraft orbiting Earth and the EUVM experiment (Eparvier et al. 2015) on the Maven mission at Mars. The orbits of Mars and 67P were such that MAVEN and *Rosetta* were on the same side of the Sun during most of the *Rosetta* mission, although there are times when *Rosetta* is better aligned with the TIMED/SEE at Earth, with the added benefit of superior wavelength resolution.

We use three independent techniques for estimating the maximum photoemission current of a negatively charged probe, the photosaturation current ( $I_{\text{ph0}}$ ), one of these techniques is to our knowledge new.

In Section 2, we go through the relevant theory of Langmuir probes and the photoelectric effect, followed by a description of each technique to obtain the photoemission current from the probes as

\* E-mail: frejon@irfu.se

well as the estimates from UV observations. In Section 3, we present our results, discuss their implications in regards to attenuation of gas and dust or contamination in Section 4, followed by conclusions in Section 5.

## 2 METHODS

Conductive objects such as the Langmuir probes on *Rosetta* will emit electrons when subjected to sunlight due to the photoelectric effect. For cases when none of the electrons are reabsorbed by the probe, such as a negatively charged probe, the photosaturation current  $I_{\text{ph}0}$  can be observed. The theory behind Langmuir probe measurements is described in Section 2.1, and three different techniques to observe  $I_{\text{ph}0}$  is described in Sections 2.2–2.4. We also propagate the UV observations around Earth and Mars to the *Rosetta* position, as described in Section 2.5.

### 2.1 Langmuir probe photoemission and probe theory

A fundamental mode of operation of a Langmuir probe is the bias voltage sweep. During a sweep, the probe is measuring the current to the probe while stepping through a series of bias voltages  $V_b$  set with respect to the spacecraft ground. The absolute potential  $V_p$  between the probe and a plasma at infinity is thus  $V_p = V_b + V_S$ , where  $V_S$  is the spacecraft potential. The current to the probe can be separated into three parts: ion ( $I_i$ ), electron ( $I_e$ ) and secondary electron emission current. The secondary emission current can be subsequently separated into photoemission ( $I_{\text{ph}}$ ) and secondary electron emission from particle impact ( $I_{\text{SEEP}}$ ). Akin to the photoemission current,  $I_{\text{SEEP}}$  will depend on material properties of the probe but is also directly proportional to the ion and electron current to the probe such that if  $I_e = I_i = 0$ ,  $I_{\text{SEEP}} = 0$ , and can in most cases be assumed to be negligible.

It can be shown (Mott-Smith & Langmuir 1926; Medicus 1961) that the electron current to a spherical probe is given by

$$I_e = \begin{cases} I_{e0} \left(1 + \frac{eV_p}{k_B T_e}\right) & \text{for } V_p \geq 0 \\ I_{e0} \exp\left(\frac{eV_p}{k_B T_e}\right) & \text{for } V_p < 0, \end{cases} \quad (1)$$

where  $I_{e0}$  is the random current for electrons, given by

$$I_{e0} = A_p e n \sqrt{\frac{k_B T_e}{2\pi m_e}}, \quad (2)$$

where  $n$  is the plasma density,  $T_e$  is the electron temperature and  $A_p$  is the surface area of the Langmuir probe and other constants have their usual meaning.

For supersonic ion flow of single positive charge, the ion current to a sphere is shown by Fahleson, Fälthammar & Pedersen (1974) to be

$$I_i = \begin{cases} -I_{i0} \left(1 - \frac{eV_p}{E_i}\right) & \text{for } V_p < E_i/e \\ 0 & \text{for } V_p > E_i/e, \end{cases} \quad (3)$$

where  $E_i = \frac{m_i u^2}{2}$  is the energy of ions of mass  $m_i$  and flow speed  $u$ ,  $I_{i0}$  is the ram current, given by

$$I_{i0} = A_c e n u, \quad (4)$$

where  $A_c$  is the circular cross-section of the probe.

For a negatively charged probe, the photoemission current is then at its saturation value  $I_{\text{ph}0}$  which depends on the UV sun flux  $F(\lambda)$  at each wavelength  $\lambda$ , the surface area normal to the sunlight  $A_c$ , as well as the photoelectron yield PEY( $\lambda$ ) of the probe material, defined as

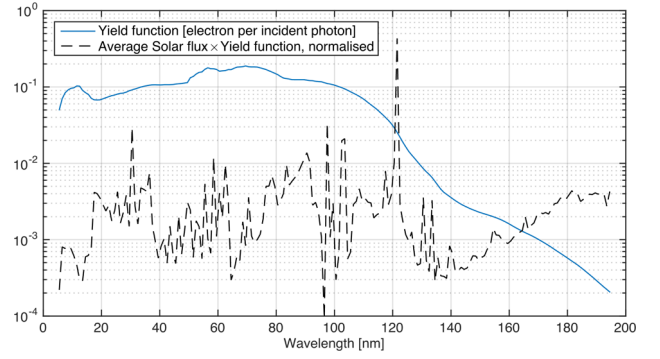


**Figure 1.** Photoelectric yield in electrons per incident photon (solid line) versus wavelength adapted from Feuerbacher & Fitton (1972) and Canfield & Swanson (1987), used to estimate photoemission from the probe from the two EUV data sets. The fractional current contribution of the typical value of each solar flux wavelength (dashed line) is also plotted for reference.

number of emitted electrons per incident photon. Following Grad (1973), and defining  $F(\lambda)$  to be in units of photons  $\text{s}^{-1}\text{m}^{-2}$ , we obtain

$$I_{\text{ph}0} = -A_c \int \text{PEY}(\lambda) F(\lambda) d\lambda. \quad (5)$$

In the absence of photoelectron yield measurements for TiN, we follow the approach inspired by Brace et al. (1988) and Hoegy et al. (1993) in a similar situation. They used a yield function adapted from an average of metals examined by Feuerbacher & Fitton (1972) and Canfield & Swanson (1987) with a free numerical factor to scale the estimated photosaturation current from equation (5) to the measured photoemission, using sun flux measurements of other spacecraft. In our case, the free numerical factor turned out to be very close to 1 between the MAVEN/EUVM UV spectra and our photoelectron yield. We therefore adopted the yield function plotted in Fig. 1 with no further tuning or correction.

TIMED/SEE spectral irradiance data include uncorrected degradation beginning in late 2011, resulting in irradiances which become increasingly lower with time than those measured by other spacecraft (SDO/EVE). Therefore, the free numerical factor differed from 1 when we used TIMED/SEE data.

### 2.2 Probe photoemission current from sun–shadow transitions

The component of the total probe current due to photoemission from the probe surface,  $I_{\text{ph}}$ , clearly vanishes for a probe which is not sunlit. Therefore, an obvious way of measuring the photoemission current of a probe is by comparing the probe current at fixed voltage-bias just before and after it goes into or out of shadow. This seemingly straightforward method requires at least two conditions to be met: (1) the probe must be at a negative potential w.r.t. the local plasma at the position of the probe in order for the full photosaturation current  $I_{\text{ph}0}$  to be sampled, limiting the data set to probe sun–shade transitions during which LAP1 is commanded at a negative bias potential w.r.t. the spacecraft; (2) concurrent variations in probe current due to other factors, e.g. varying plasma density, temperature, drift velocity, etc., must be either negligible in comparison to the photoemission current, or occur on sufficiently short time-scales that their effects can be filtered out. In practice, this limits the applicability of the method to probe sun–shade transitions which are sufficiently fast for the general background ion current to be essentially a stationary process, but at the same time separated by sufficient time for calculation of statistical moments of this

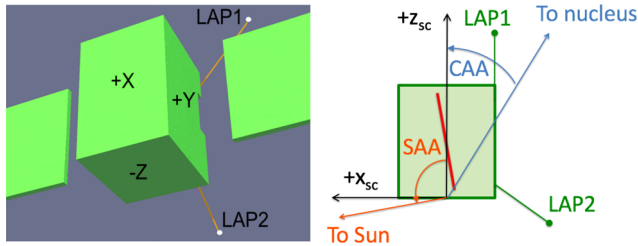


**Figure 2.** Left: 3D-visualization of the *Rosetta* spacecraft with the two Langmuir probes LAP1 and LAP2. Right: geometry visualization and definition of SAA and Comet Aspect Angle (CAA), solar panels marked in red. When the spacecraft box turns around its  $Y$ -axis, LAP1 goes in and out of shadow behind the  $+Y$  Solar array for a certain range of SAA.

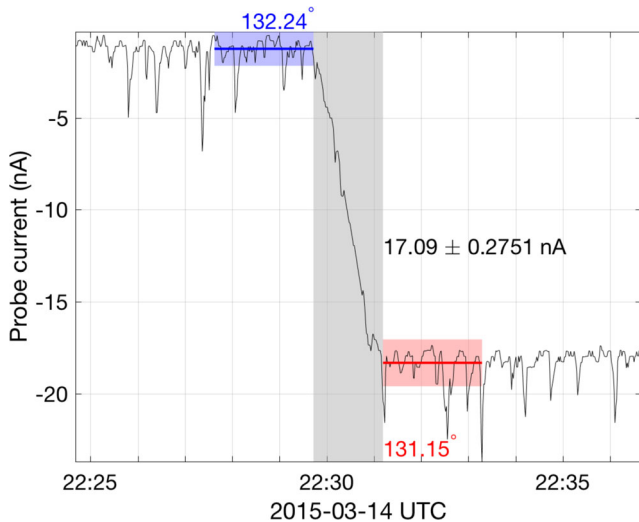


**Figure 3.** Example of shadow crossing  $I_{\text{ph}0}$  estimate from current level shift when crossing into shadow for a negatively charged probe.

process, e.g. arithmetic mean and standard deviation. We have in this study decided to use only probe sun–shade transitions in which the probe goes from completely sunlit to completely shaded, or vice versa, in no more than 2 min, preceded and succeeded by periods of complete sunlight or shade for at least 2 min.

Fig. 2 (left) shows a sketch of the *Rosetta* spacecraft and RPC-LAP. The solar panels were almost always held orthogonal to the Sun, meaning the  $S/C$   $Y$ -axis stayed perpendicular to the Sun. When the spacecraft turned around its  $Y$ -axis, which happened regularly, LAP1 would become completely shadowed by the spacecraft solar array. In Fig. 2 (right), we define the Solar Aspect Angle (SAA), as the angle between the spacecraft  $+Z$  and the direction of the Sun, counted positive when the Sun moved from  $+Z$  towards  $+X$ .

Fig. 3 shows an example from 2015 March 3 where LAP1 goes from shadow to sunlight. The actual sun–shade transition, during which the probe is partially sunlit and hence draws a successively increasing photoemission current, is marked by the grey patch in the figure. The SAAs at which the probe enters and exits partial illumination conditions are shown in the figure; they are  $132^{\circ}2$  and  $131^{\circ}2$ , respectively. For LAP1, there is also a second possible transition region between  $178^{\circ}2$  and  $179^{\circ}2$  which is also used in this study, when available. For visual reference, see Fig. 2.

The magnitude of the current jump across the transition region is calculated by taking the difference of the arithmetic means of the probe current during the 2-min periods immediately preceding and succeeding it, shown as blue and red lines, respectively, in Fig. 3. As

can be seen in Fig. 3, the probe current is prone to brief pulses of considerably increased magnitude. These have been interpreted as cold plasma filaments passing by the spacecraft (Eriksson et al. 2017) and produce a substantially skewed distribution about the mean of the sample currents. Therefore, following Tukey (1977), all sample currents which lie more than 1.5 times the interquartile range below the first quartile or above the third quartile are discarded as outliers.

Sample standard deviations  $\sigma_{\text{before}}$  and  $\sigma_{\text{after}}$  are computed taking into account sample auto-correlation using the method of Zieba (2010) (specifically their equation 10). Corresponding confidence intervals at the 95 per cent level,  $1.96\sigma/\sqrt{n}$ , with  $n$  the number of samples, are shown in Fig. 3 as blue and red shaded regions, respectively. A confidence interval for the difference of the means is then simply obtained as  $1.96\sqrt{\sigma_{\text{before}}^2/n_{\text{before}} + \sigma_{\text{after}}^2/n_{\text{after}}}$ .

This method for measuring the probe photoemission current has the advantage of being unaffected by any potential additive offsets in the current measurements, since it relies on a current difference and not on the absolute value. Its main shortcoming is that its application is contingent on specific attitude and commanding criteria, as previously mentioned, and as thus a rather sparse and uneven data set. During the entire autumn of 2014, there is not a single sun–shade transition of LAP1 coinciding with commanded negative fixed bias voltage. This situation was somewhat remedied by the fact that the ion current in the frequent sweeps during this time of low cometary activity far away from the Sun was entirely negligible compared to the photoemission current. Therefore, photoemission estimates from 2014 August to October were obtained from the difference of the currents at large negative bias voltages between sweeps immediately before and after a sun–shade transition. Specifically, we obtain arithmetic means and standard deviations from the currents at the lowest 5 V of bias potentials in each sweep, allowing us to estimate confidence intervals of the photoemission current for each transition.

### 2.3 Probe photoemission from single sweeps

Throughout the *Rosetta* mission, the Langmuir probe instrument has seen a very dynamic and varying plasma with regions where ion, electron and photoemission current have, within the bias voltage range of the *Rosetta* Langmuir probe, each individually dominated the Langmuir probe sweep measurement (Eriksson et al. 2017). For sunlit probes, an automatic routine was set to find the knee  $V_{\text{ph}}$  in the  $I-V$  curve, as previously described by Odelstad et al. (2017), and by proxy,  $V_{\text{S}}$ , to subdivide the  $I-V$  curve into two regions of  $V_{\text{p}}$ . Assuming the spacecraft potential is well within the voltage bias sweep of  $\pm 30$  V, the two regions will be characterized by the linear ion current and the photosaturation current for  $V_{\text{p}} < 0$  and a linear electron current for  $V_{\text{p}} > 0$ . Using the fact that at  $I(V_{\text{p}} = 0) \approx I_{\text{e}0} + I_{\text{i}0}$  from equations (1) and (3), we use an automatic fitting routine to remove a model of the electron and ion current component to obtain only the current contribution from  $I_{\text{ph}}$  and  $I_{\text{SEEP}}$ . The latter can be assumed to be negligible for all but the densest of plasmas, such that for negative  $V_{\text{p}}$  we can obtain  $I_{\text{ph}0}$ . An example of the sweep current fitting routine result is shown in Fig. 4.

The accumulated errors from a single estimate with this technique is expected to be large, owing to the many mutually dependent fits needed to procure the estimate, as well as the noise level of the instrument. Indeed, there are times where the automatic routine does not produce physically meaningful results, and as such only 92 per cent of the data set was used due to inexactness of the automatic routine, interference or erroneous commanding. The automatic routine and the threshold of validity used are still in development, so to limit the

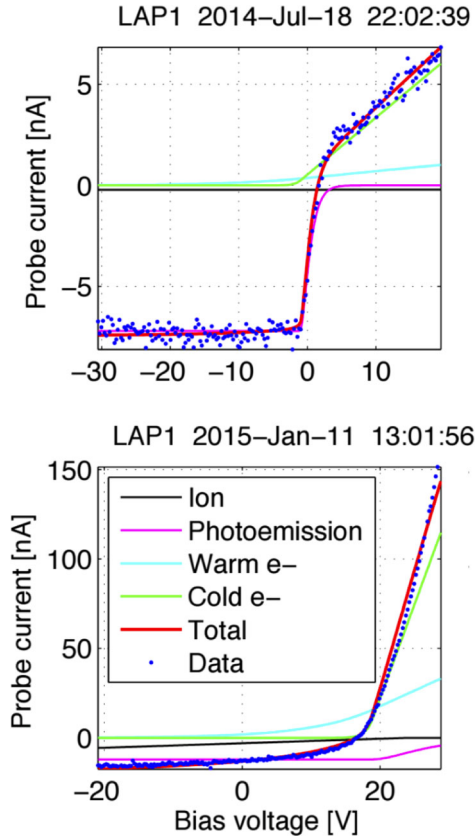


**Figure 4.** Example RPCLAP  $I$ - $V$  curve data (blue) and photoemission (pink) model for two different plasma regions of tenuous (top) and dense (bottom) plasma, figure courtesy of Eriksson et al. (2017).

impact of erroneous estimates, we present the median result over an operational block, defined as a period when the instrument is operated in one single operational mode (on average 400 measurements over 3–4 h), and the Median Absolute Deviation (MAD) in Fig. 6.

The largest source of random error is estimated to arise in the electron model fit, in a region where we often see a non-well-behaving current, as well as the difficulties of correctly estimating  $V_S$ , as studied in greater detail by Odelstad et al. (2017). However, as the sample size is very large (around 400 000), we expect to become much less sensitive to random errors as we take a median of the results. Of all uncertainties involved, the dominant source is expected to be the possible systematic error from secondary emission current which may give exaggerated values of  $I_{ph0}$ . If there is a discrepancy between this result and other  $I_{ph0}$  estimates, we may be able to estimate the impact of secondary electron emission from particle impact on the Langmuir probes.

#### 2.4 Probe photoemission from analysis of multiple sweeps

Assuming that the photoemission from the probe does not change significantly between sweeps, it is possible to find the photoemission current by combining results from several sweeps. For this purpose, data from the ion saturation region is required, so that the electron current can be taken as negligible. Taking  $eV_p/k_B T_e \ll -1$ , the total current, assuming no secondary emission by particle impact, detailed in Section 2.1 simply reduces to

$$I_{tot} \approx I_i + I_{ph0}, \quad (6)$$

and the derivative is then

$$\frac{dI_{tot}}{dV_p} = \frac{dI_i}{dV_p}.$$

This result combined with equations (3) and (6) yields

$$\frac{dI_{tot}}{dV_p} = k (I_{tot} - I_{ph0}) \propto \frac{n}{u}, \quad (7)$$

where  $k$  is given by

$$k = \frac{e}{eV_p - E_i}.$$

Assuming that  $k$  does not change during the sweeps, we can extrapolate for  $I_{tot}(n=0)$  from a number of measurements of  $I_{tot}$  and  $\frac{dI_{tot}}{dV_p}$  with enough spread in  $n$ , as

$$\frac{dI_{tot}}{dV_p}(n=0) = 0 \Rightarrow I_{tot} \approx I_{ph0}. \quad (8)$$

Although we have so far ignored  $I_{SEEP}$ , we note that for electron emission from ion impact, if it increases linearly with density and for  $eV_p \ll E_i$  it would be indistinguishable from the ion current and would not affect equation (8). For other values of  $E_i$ , it would introduce a small non-linear current slope as the energy of primary collision species increases. Also, as the primary electron current in the specified region is assumed to be negligible, so would its secondary current be. When this is not the case, the secondary current would instead slightly mitigate the effect the primary electron current would have on the photoemission estimate.

Restricted by the condition that  $k = e/(eV_p - E_i)$  needs to be approximately constant during the series of sweeps, it is worth investigating under which range of plasma parameters this method is effective. Note that in order to use equation (7) to extrapolate  $I_{ph0}$ , we need several data points from sweeps during changing plasma conditions, as illustrated in Fig. 5. Although this method is sensitive to both  $n$  and  $u$ , the plasma environment around *Rosetta* varies much faster in density, with order of magnitude density fluctuation time-scales of minutes to seconds as reported by Henri et al. (2016) as well as the diurnal variation evident by the  $V_S$  data in Odelstad et al. (2015). In comparison, the ion velocity appears much more stable (Vigren et al 2017, this issue), but will still introduce some random error. We investigate this theoretically in the appendix. In Section 3, we will find that all three methods agree well, suggesting small errors in practice.

The  $I_{ph0}$  data set from the multiple sweep method and the variance of the fit is plotted in Fig. 6, results with large variances in the linear ion slope, and as such, large non-linear effects from e.g. the electron retardation current, are discarded.

#### 2.5 Propagation of TIMED/SEE and MAVEN/EUVM data to *Rosetta*

*Rosetta* does not carry any instrument for direct measurement of solar UV flux at the position of the spacecraft. For comparison, we rely on measurements from TIMED/SEE at Earth and MAVEN/EUVM at Mars, propagated out to the position of 67P. The propagation procedure consists of finding the last preceding and first succeeding epochs at which the ‘source’, Earth or Mars, respectively, was at the same solar longitude as that of *Rosetta* at the queried epoch. The measured UV flux at these epochs are then scaled by the square of the respective heliocentric distances of the source divided by that of *Rosetta* at the queried epoch. Finally, a weighted average of the two scaled EUV measurements at the source is computed such that

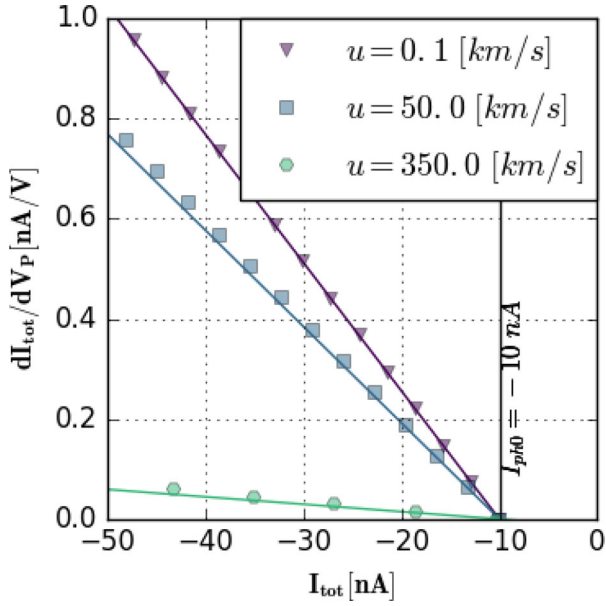


**Figure 5.** Slope versus  $I_{\text{tot}}$ . For several sweeps at different plasma densities, a linear fit of the ion current and slope will yield an estimate of  $I_{\text{ph0}}$  when the fit crosses the  $x$ -axis. Triangle, square and circle points are taken from synthetic data sweeps with  $T_e = 5$  eV,  $V_S = -10$  V and varying  $n$  for three different ion velocities, and the solid lines are calculated from equation (7). There is a good agreement between the synthetic data and equation (7). Small deviations are related to high plasma densities, where  $I_e$  becomes significant.

the value of the closest measurement taken less than a few days before or after the queried epoch was used, otherwise the two values are weighted together by a linear interpolation of their respective temporal separation from the queried epoch.

The data sets used for the propagation are Level 3 daily averages from the TIMED/SEE data base (Woods et al. 2005) and Level 3 daily averaged spectral irradiance (non-flare background data) from MAVEN/EUVM (Thiemann et al. 2017a) and the propagated results are plotted in Fig. 6. The shaded regions in Fig. 6 a correspond to periods where Mars (purple) and Earth (green) were within a  $45^\circ$  azimuth sector of *Rosetta* in the elliptical plane, where we expect optimal correlation. It should be noted that Mars never was further than  $72^\circ$  behind *Rosetta* until 2016 July.

### 3 OBSERVATIONS

All three methods to obtain the photosaturation current correlate well with each other both on the global scale and the small scales in Fig. 6a, resolving the solar sidereal rotation period of  $\approx 24.5$  d. In particular, the good agreement between the three different methods verifies the methods and suggests that we are not heavily influenced by the many individually unique error sources for each method.

The two EUV photoemission estimates derived from MAVEN/EUVM and TIMED/SEE data agree over the entire period with negligible differences between them if we scale the TIMED/SEE data by a factor of 1.2, in an attempt to correct for the known degradation on TIMED/SEE since late 2011. The scaling could also be analogous of a slightly larger photoelectron yield, and is still very reasonable from the photoelectron yield data set (Feuerbacher & Fitton 1972).

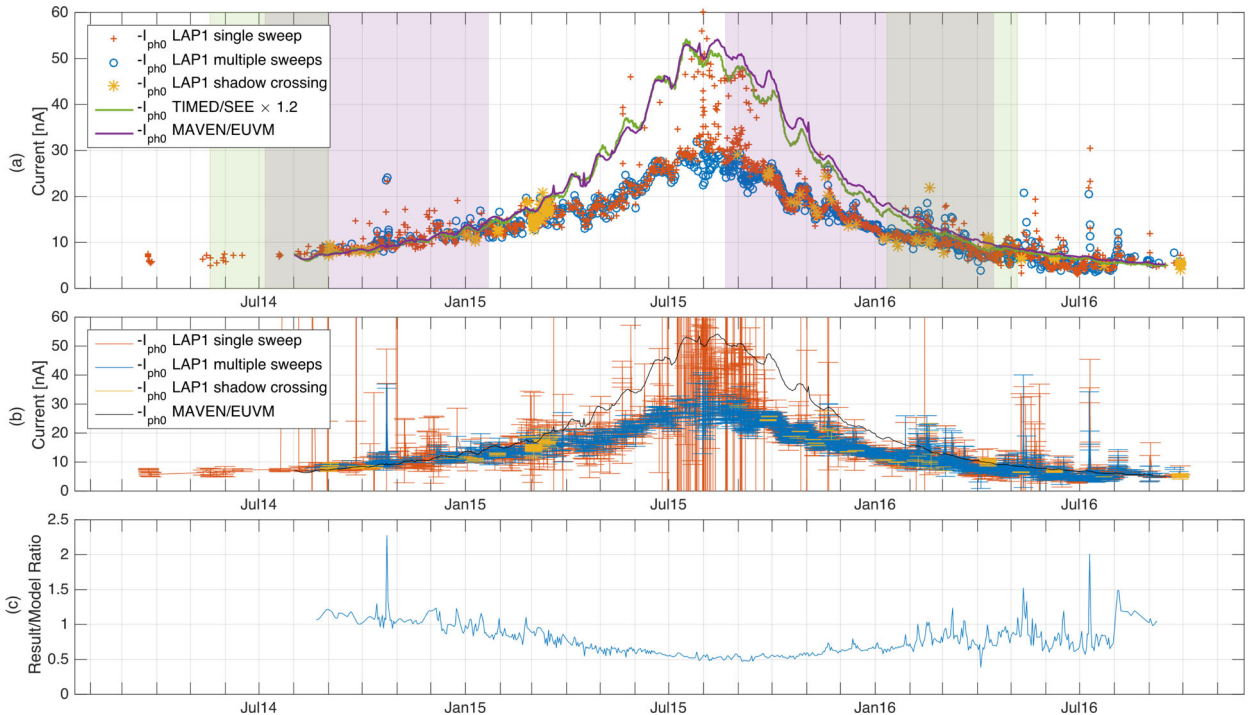


**Figure 6.** Top: photosaturation current and estimated photoemission current from EUV data from 2014 March to 2016 September. The shaded regions correspond to periods where Mars (purple) and Earth (green) were within a  $45^\circ$  azimuth sector of *Rosetta* in the elliptical plane, where we expect optimal correlation. The  $I_{\text{ph0}}$  estimate from TIMED/SEE EUV data was scaled to align with the MAVEN/EUVM data set with a factor of 1.2. Middle: result and variance of the three different methods used, and the MAVEN/EUVM  $I_{\text{ph0}}$  estimate for reference in black. Periods of large variance coincide with solar flares for the multiple sweep method and both flares and comet activity for the single sweep method. Bottom: ratio between LAP1 multiple sweep method  $I_{\text{ph0}}$  result and  $I_{\text{ph0}}$  MAVEN/EUVM model, interpolated to one estimate per day.

The photosaturation current obtained from single sweeps cannot distinguish between secondary emission from photon or particle impact, and around perihelion (2015 Aug), where we expect high densities and collisions to be more frequent, we obtain a much higher estimate than the other methods at certain points. As evident by the large variance of these points in the single sweep method in Fig. 6b, the uncertainties at perihelion are large, and as such, these points of the single sweep method data should be ignored. However, subtracting the single sweep  $I_{\text{ph0}}$  estimates from the multiple sweep  $I_{\text{ph0}}$  estimates, we could obtain estimates of the secondary emission from particle impact from the probe (although not done in this report). This is otherwise impossible to observe directly with LAP. We can also use this to estimate when we safely can assume impact emission to be negligible.

Also evident in the result and variance of the  $I_{\text{ph0}}$  data are brief large-amplitude changes of photoemission, which upon inspection correlate with solar flares (e.g. X1.6 flare 2014-10-22, M4.5 flare 2015-11-20).

The mission typical 30–160 s cadence of the Langmuir probe sweep is in theory more than enough for detecting most flares in EUV (Aschwanden et al. 2014; Veronig et al. 2002). However, individual probe sweeps may have significant noise, due to the plasma conditions and other error sources, complicating such detection. More than anything, the processing (binning, averaging) of the data set in this report limits the detection to Long Decay Events (LDEs) with durations on the order of hours, typically reserved for the largest GOES X-ray flare classes (X and M) (Aschwanden & Freeland 2012). In a study by Aschwanden et al. (2014), they conclude that their channel of largest wavelength, 30.4 nm is the optimal for detecting flares in the EUV. As seen in Fig. 1, the RPC-LAP probes can be expected to have good sensitivity to these wavelengths.

## 4 DISCUSSION

As can be seen in Fig. 6c, the UV flux derived from probe photoemission is about as expected at the start and end of the mission, but smoothly drops to about half its expected value around perihelion. There seems to be some shortfall also at end of mission, but data variability here is much more pronounced. Nevertheless, it is clear that the photoemission has a drop around perihelion, from which it at least partially recovers as *Rosetta* follows the comet outwards.

We will discuss possible explanations of this photoemission decrease including contamination in Section 4.1 and attenuation by comet gas or dust in Sections 4.2 and 4.3, but we note first that: (1) the orbital inclination of Comet 67P of  $7^\circ$  from the planetary ecliptic plane, would give us a slightly different Sun flux than measured by MAVEN/EUVM or TIMED/SEE, but the effect would be limited and much less than observed; (2) the good agreement for all three methods suggests that we are not significantly affected by offsets and unique individual error sources; (3) the uncertainty in the photoelectric yield of TiN may affect the estimated  $I_{\text{ph0}}$  on small scales, but even a vastly different yield profile would not change the deviation around perihelion since there is no significant trend in any wavelength channel which influences the result other than the  $r^{-2}$  dependence over the course of the mission.

### 4.1 Contamination

Effects on the probe surface such as contamination, which could introduce a resistance and a net reduction in emitted current, would either be expected to be cumulative over the entire mission or be

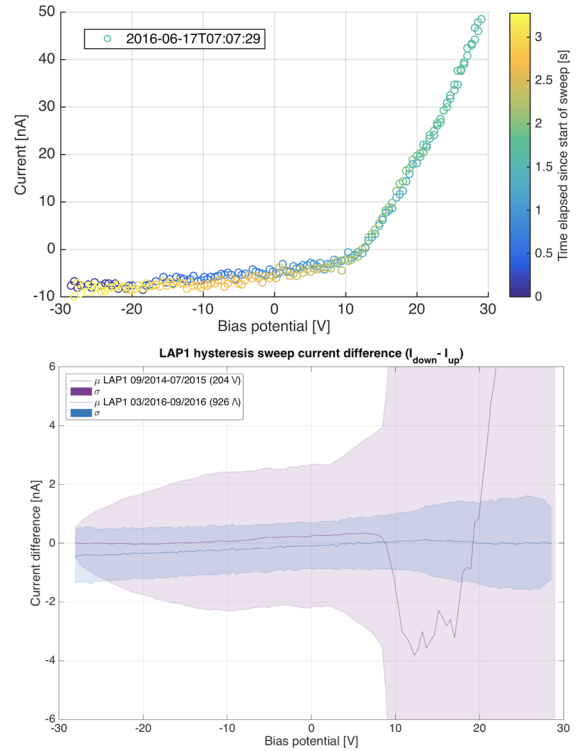


**Figure 7.** Top: example LAP1 hysteresis up-down sweep from blue to green to yellow. Bottom: hysteresis sweep analysis during the comet phase of the mission divided into two data sets with different sweep parameters. Averages and standard deviation of down-up sweeps during 2014–2015 in purple, and up-down sweeps (2016 data) in blue.

less during periods when the comet–spacecraft distance is large such as the day-side (2015 Sep–Oct) or night-side excursion (2016 Mar–Apr). In addition, a contamination in form of a resistive and capacitive layer should be discernible when alternating bias stepping direction (hysteresis sweeps) according to Szuszczewicz & Holmes (1975):

$$\Delta I = \frac{C \Delta V_b}{\Delta t}$$

where  $\Delta t$  is the time between two subsequent current measurements  $\Delta I$  on a probe with a capacitance  $C$ .

To monitor contamination on the Langmuir probes, more than 23 000 hysteresis sweeps were performed throughout the mission. A summary for LAP1 is plotted in Fig. 7, subdivided into two data sets with different starting potentials and time periods. The sweeps are either from  $-30$  V up to  $+30$  V and back down to  $-30$  V (‘up-down’) or vice versa (‘down-up’).

As evident by the large variance (up to 400 nA, off scale) for the first set of sweeps, the electron current to the probe changes rapidly in comparison to the sweep duration ( $\approx 6$  s), such that the method was changed during 2016 to an up-down type of sweeps, with clearer results. We find no significant capacitive current contribution, but estimate that at most it would offset our results in the two sweep analysis methods with  $0.3 (\pm 0.5)$  nA, and is as such negligible. The sun–shadow transition data are unaffected by this capacitive current offset.

On LAP2, we do find evidence of significant contamination, particularly during a few months after the day-time excursion in 2015 Oct with a capacitive current contribution exceeding 20 nA,

as well as a significant decrease in photoemission current. The LAP2 results are therefore excluded from this report.

#### 4.2 Attenuation by comet gas

As observed by the *Rosetta* Alice instrument (Keeney et al. 2017), the neutral gas and dust of the comet coma can absorb a large (>50 per cent) fraction of some spectral lines in the 70–200 nm range of Alice observation. In particular, the common comet gas species of interest with substantial absorption cross-sections within our yield profile would be H<sub>2</sub>O, CO<sub>2</sub> and CO. However, Alice absorption observations are along a path close to the comet core, with regions of peak densities, whereas the probe-Sun path are almost always along more tenuous atmosphere profile due to the terminator plane or day-side orbit of *Rosetta*, and as such very sensitive to the *Rosetta*–comet distance  $d_{CG}$ , which was above 200 km for several months around perihelion. We have applied the method of Vigren & Galand (2013) to estimate a maximum EUV absorption of only 0.8(±0.1) per cent by H<sub>2</sub>O molecules near perihelion at  $d_{CG} = 330$  km (the attenuation was calculated along the Sun–*Rosetta* line assuming a spherically symmetric coma decaying in number density as  $d_{CG}^{-2}$ ). In the same scenario but close to the comet surface, the maximum EUV absorption is instead 70(±7) per cent at certain wavelengths, and as such not in disagreement with Alice results. Unfortunately there are no direct measurements of incident solar UV from Alice or other *Rosetta* instruments, and we lack an absolute measure of the incident solar UV at *Rosetta* to compare with the RPCLAP photoemission.

#### 4.3 Attenuation by cometary dust

Another possible source of EUV extinction would be scattering and absorption of cometary dust grains. Studies on interstellar dust by Cruise (1993) and Kolokolova et al. (2004) indicate that EUV scattering by micrograins and nanograins can be significant. Even so, the large dust grains mainly observed by the GIADA, COSIMA and MIDAS dust instruments (Fulle et al. 2015; Rotundi et al. 2015; Bentley et al. 2016; Hilchenbach et al. 2016) could not, for the amounts reported, provide sufficient surface area for our inferred UV decrease of 50 per cent at perihelion. However, the particles investigated with the MIDAS instrument all show agglomerate character with subunit sizes down to the nanometre scale. It is therefore conceivable that cometary dust particles could undergo a process like fragmentation or erosion which leads to the release of their constituent (nano)grains, thus increasing the total surface area and more significant attenuation in UV may result.

If the nanograin production would be most efficient farther away than *Rosetta*'s position from the comet nucleus, this would explain the absence of a large UV extinction difference for different *Rosetta*–comet distances (which were, e.g. between 200 and 1000 km in 2015 Oct). It is notable that the first direct detections of nanograins at a comet were made during the fly-by at 1P/Halley, which covered distances that were mainly larger than the general *Rosetta*–comet distance, and that there are measurements suggesting high densities of nanograins at immense (in the order of 10<sup>6</sup> km) comet distances (Utterback & Kissel 1990).

From *Rosetta* at 67P, nanograins were occasionally detected by the Ion and Electron Spectrometer IES (Burch et al. 2015) and seen to flow mainly in the antisunward direction. In addition, the GIADA dust detector noted a three times higher flux of submicron dust particles in the antisolar direction than the flux coming directly from the nucleus (Della Corte et al. 2015). Gombosi, Burch &

Horányi (2015) modelled the influence of radiation pressure on grain motion, suggesting nanograins originate from larger grains emitted by the comet and fragmenting at distances of several (tens of?) thousand km sunward of the nucleus. The radiation pressure drives them back towards the comet as seen by IES and GIADA, also yielding a significant nanograin column density in the sunward direction from *Rosetta* as suggested in our scenario.

In the following, we will test if our hypothesis of nanograins absorbing the EUV coming from the Sun can hold. We will check if fragmentation or erosion of a minor amount of dust particles at large distance from the nucleus can lead to a sufficient population of nanograins and estimate the necessary size to account for our observations. We will revisit *Rosetta* results to ensure their compatibility, and finally discuss the implications of a hypothetical existence of a nanograin population in a certain distance of the comet.

Consider large (1–1000 μm) grains being produced at the comet surface, ejected isotropically at some velocity  $u$ , and fragmenting or eroding into smaller particles of radius  $a$  outside some distance  $d_0$ , scattering 100 per cent of their spherical geometric cross-section such that the fraction of scattered light  $\alpha_s$  is

$$\alpha_s \in [0, 1] = N \pi a^2, \quad (9)$$

where  $N$  is the column density of spherical dust grains small enough for significant UV absorption. This assumes the fraction of scattered light, or the optical depth, to be small and for a more general case we note that equation (9) becomes

$$-\ln(1 - \alpha_s) = N \pi a^2. \quad (10)$$

If we let a fraction  $f_{\text{frag}} < 1$  of the total mass of the dust cloud undergo fragmentation or erosion, then the total mass  $M$  per area  $A$  of dust in a column between *Rosetta* and the Sun becomes

$$\frac{M}{A} = \frac{N m_g}{f_{\text{frag}}} = \frac{4\pi a^3 \rho N}{3 f_{\text{frag}}},$$

where  $m_g$  is mass of a dust grain fragmentation product of density  $\rho_{\text{frag}}$ . Inserting equation (9) gives

$$\frac{M}{A} = \frac{4a \rho \alpha_s}{3 f_{\text{frag}}}. \quad (11)$$

In a column from  $d_0$  to the Sun, where we assume the dust grains have fragmented into small enough particles for significant UV scattering to take place, the mass per area is then

$$\frac{M}{A} = \int_{d_0}^{\text{Sun}} \rho_{\text{vol}}(r) dr = \rho_0 \int_{d_0}^{\text{Sun}} \left(\frac{R}{r}\right)^2 dr \approx \frac{\rho_0 R^2}{d_0}, \quad (12)$$

assuming an isotropic density distribution decreasing with  $r^{-2}$  from the comet surface at  $r = R$ , where the volume average mass density of dust  $\rho_{\text{vol}}(R) = \rho_0$ .

Assuming a constant dust-to-gas mass ratio  $C$ , we can use the production rate  $Q$  of water gas from Hansen et al. (2016), to estimate  $\rho_0$ :

$$\rho_0 = \frac{m_g Q_{\text{dust}}}{4\pi R^2 u} = \frac{C m_{\text{H}_2\text{O}} Q_{\text{H}_2\text{O}}}{4\pi R^2 u} \quad (13)$$

Finally, by combining equations (11)–(13) we obtain:

$$\frac{4a \rho \alpha_s}{3 f_{\text{frag}}} = \frac{C m_{\text{H}_2\text{O}} Q_{\text{H}_2\text{O}} R^2}{4\pi R^2 u d_0},$$

solving for  $a$  yields

$$a = \frac{3 f_{\text{frag}} C m_{\text{H}_2\text{O}} Q_{\text{H}_2\text{O}}}{16\pi u d_0 \alpha_s \rho}. \quad (14)$$

At perihelion for a dust grain with average outflow velocity  $u = 3 \text{ m s}^{-1}$  as reported by Fulle et al. (2015), dust bulk density  $\rho = 800 \text{ kg m}^{-3}$  (Rotundi et al. 2015), dust-to-gas mass ratio  $C = 5$  (Snodgrass et al. 2016),  $Q_{\text{H}_2\text{O}} = 3.5 \times 10^{28} \text{ s}^{-1}$  (Hansen et al. 2016), and letting  $f_{\text{frag}} = 10$  per cent of the dust mass fragment and absorb  $\alpha_s = 50$  per cent of incoming EUV in a column from  $d_0 = 1000 \text{ km}$  to the Sun, we estimate the dust grain radius to be  $\approx 19 \text{ nm}$ .

A spherical dust grain with radius of 19 nm would according to Skolnik (1981) scatter 100 per cent of its geometric cross-section of light in wavelength of  $2\pi a = 119 \text{ nm}$  and below, and is as such on the correct length-scale for attenuation in RPC-LAP wavelengths. The above considerations are of course very rough, resting on a series of assumptions. Nevertheless, they show that the above hypothesis cannot be ruled out directly. An obvious simplification in the model is the singular size of the disintegration product. A size distribution, although useful, should be cemented in a firm understanding of the disintegration process involved, including disintegration products and forces, which we do not pretend to have. However, if the simple model works for a singular size of grains, then it will also work for some distribution of grains. Furthermore, due to our lack of physical model for the disintegration,  $d_0$  is more or less a free parameter. However, we chose a value consistent with (1) a negligible decrease of attenuation even during the day-side excursion (2015 Sep–Oct, up to 1000 km sunward), (2) remote observations (Boehnhardt et al. 2016) of 67P dust, discussed in more detail below and (3) still much less than the apex distance for dust grains as investigated by Gombosi et al. (2015).

To compare these results with other *Rosetta* observations, it should be noted that the presented RPC-LAP measurements were taken by remotely sampling the *Rosetta*–Sun environment. *Rosetta* carried a variety of other remote instruments, although most investigated the vicinity of the comet nucleus and rarely sampled sunward. Additionally, the different spectral ranges of the instruments further impede a detection of UV-extinction as, e.g. the scientific camera system on-board OSIRIS is sensitive in the range of 250–1000 nm (Keller et al. 2007), for which the geometric scattering efficiency of 19-nm-sized nanograins would decrease to 4–0.1 per cent (Skolnik 1981) and thus possibly escape detection.

As stated in the beginning of this section, the amounts reported in direct observations of large dust grains cannot directly account for the inferred UV attenuation. Our model thus relies on a mechanism of fragmentation or erosion of large grains at larger distances than the typical *Rosetta*–comet distance. One such mechanism would be erosion and/or evaporation of gluing material (Lasue et al. 2007; Boehnhardt et al. 2016). As this process would be most effective for periods with high solar radiation, it would readily account for the strong UV absorption during perihelion whilst fading to absence for increasing comet–Sun distances. This scenario is also in agreement with remote observations of comet 67P from Earth by Boehnhardt et al. (2016), where their observational data suggest dust fragmentation at large comet distances, in particular for perihelion when the vicinity of the comet to the Sun facilitates dust heating and thus material degradation. Furthermore, the modelling work of Gombosi et al. (2015) shows that dust particles ejected sunward may be deflected by solar radiation at a comet distance of some thousand kilometres, and suggest particle fragmentation close to their turn-around point. Finally, as comets are speculated to be a source of nanodust in our Solar system (Mann 2017), the herein presented hypothesis might aid the understanding of the comet contribution to the Solar system dust.

## 5 CONCLUSIONS

We have presented estimates of the Langmuir probe photoemission current using three different methods of which one is, to our knowledge, new. All three methods agree very well on global and small scales and enables the use of the Langmuir probe as an ultraviolet photodiode on *Rosetta*. The three methods are further validated by the use of theoretical estimates of the Langmuir probe photoelectron emission using EUV measurements from two other spacecrafts, and a suitable estimate for the photoelectron yield of the titanium probe, which agrees very well on the start and end of the mission as well as small-scale fluctuation in solar sidereal rotation frequencies. The results in this paper can be used to estimate the solar EUV intensity at the *Rosetta* position, as well as cataloguing flares. We also report a significant current discrepancy from our measured values to the EUV estimates around perihelion, correlating with high cometary activity. Although there are many sources of errors of any method individually, only contamination is common between all three methods, of which no evidence has been found. Attenuation by gas emitted from the nucleus cannot explain the decreased photoemission. However, a test model of attenuation by erosion or fragmentation of dust creating grains of tens of nanometres far from the comet is found to be consistent with observations.

## ACKNOWLEDGEMENTS

*Rosetta* is a European Space Agency (ESA) mission with contributions from its member states and the National Aeronautics and Space Administration (NASA). This work has made use of the Automated Multi Dataset Analysis (AMDA) and Rosetta Plasma Consortium Quicklook database, provided by a collaboration between the Centre de Données de la Physique des Plasmas (supported by Centre National de la Recherche Scientifique (CNRS), Centre national d'études spatiales (CNES), Observatoire de Paris and Université Paul Sabatier, Toulouse), and Imperial College London (supported by the United Kingdom Science and Technology Facilities Council). Support by the Swedish National Space board is acknowledged, including contracts 109/12, 135/13, 166/14 and 168/15. The work at the University of Oslo is partly supported by the Norwegian Research Council, grant number 240000. The contribution from the Space Research Institute of the Austrian Academie of Sciences was made possible by the funding of the Austrian Science Funds FWF P 28100-N36.

## REFERENCES

- Aschwanden M. J., Freeland S. L., 2012, *ApJ*, 754, 112  
 Aschwanden M. J., Wülser J.-P., Nitta N. V., Lemen J. R., Freeland S., Thompson W. T., 2014, *Sol. Phys.*, 289, 919  
 Bentley M. S. et al., 2016, *Nature*, 537, 73  
 Bodewits D. et al., 2016, *AJ*, 152, 130  
 Boehnhardt H., Riffeser A., Kluge M., Ries C., Schmidt M., Hopp U., 2016, *MNRAS*, 462, S376  
 Brace L. H., Hoegy W. R., Theis R. F., 1988, *J. Geophys. Res.*, 93, 7282  
 Burch J. L., Gombosi T. I., Clark G., Mokashi P., Goldstein R., 2015, *Geophys. Res. Lett.*, 42, 6575  
 Canfield L. R., Swanson N., 1987, *NBS Measurement Services: Far Ultraviolet Detector Standards*. U.S. Dept of Commerce, National Bureau of Standards, Gaithersburg, MD  
 Cruise A. M., 1993, *MNRAS*, 265, 881  
 Della Corte V. et al., 2015, *A&A*, 583, A13  
 Einstein A., 1905, *Ann. Phys.*, 322, 132  
 Eparvier F. G., Chamberlin P. C., Woods T. N., Thiemann E. M. B., 2015, *Space Sci. Rev.*, 195, 293

- Eriksson A. I. et al., 2007, *Space Sci. Rev.*, 128, 729  
 Eriksson A. I. et al., 2017, *A&A*, 605, A15  
 Fahlson U., Fälthammar C.-G., Pedersen A., 1974, *Planet. Space Sci.*, 22, 41  
 Feuerbacher B., Fitton B., 1972, *J. Appl. Phys.*, 43, 1563  
 Fulle M. et al., 2015, *ApJ*, 802, L12  
 Galand M. et al., 2016, *MNRAS*, 462, S331  
 Gombosi T. I., Burch J. L., Horányi M., 2015, *A&A*, 583, A23  
 Grad R. J. L., 1973, *J. Geophys. Res.*, 78, 2885  
 Hansen K. C. et al., 2016, *MNRAS*, 462, S491  
 Henri P. et al., 2016, *EGU Gen. Assem. Conf. Abstr.*, 18, 16587  
 Hertz H., 1887, *Ann. Phys.*, 267, 983  
 Hilchenbach M. et al., 2016, *ApJ*, 816, L32  
 Hoegy W. R., Pesnell W. D., Woods T. N., Rottman G. J., 1993, *Geophys. Res. Lett.*, 20, 1335  
 Keeney B. A. et al., 2017, *MNRAS*, 469, S158  
 Keller H. U. et al., 2007, *Space Sci. Rev.*, 128, 433  
 Kolokolova L., Hanner M. S., Lvasseur-Regourd A.-C., Gustafson B. Å. S., 2004, in *Festou M. C., Keller H. U., Weaver H. A., eds, Comets II*. Univ. Arizona Press, Tucson, AZ, p. 577  
 Lasue J., Lvasseur-Regourd A. C., Fray N., Cottin H., 2007, *A&A*, 473, 641  
 Mann I., 2017, *Phil. Trans. R. Soc. A*, 375, 20160254  
 Medicus G., 1961, *J. Appl. Phys.*, 32, 2512  
 Mott-Smith H. M., Langmuir I., 1926, *Phys. Rev.*, 28, 727  
 Odelstad E. et al., 2015, *Geophys. Res. Lett.*, 42, 2015GL066599  
 Odelstad E., Stenberg-Wieser G., Wieser M., Eriksson A., Nilsson H., Johansson F., 2017, *MNRAS*, in press  
 Rotundi A. et al., 2015, *Science*, 347, aaa3905  
 Skolnik M. I., 1981, *Introduction to Radar Systems*, 3rd edn. Irwin Electronics & Computer Engineering, Vol. 3, McGraw-Hill Book Company Inc., New York, NY  
 Snodgrass C. et al., 2016, *MNRAS*, 462, S138  
 Szuszczywicz E. P., Holmes J. C., 1975, *J. Appl. Phys.*, 46, 5134  
 Thiemann E. M. B., Chamberlin P. C., Eparvier F. G., Templeman B., Woods T. N., Bougher S. W., Jakosky B. M., 2017, *J. Geophys. Res. Space Phys.*, 122, 2016JA023512  
 Tukey J. W., 1977, *Exploratory Data Analysis*, Series in Behavioral Science: Quantitative Methods, Reading, Mass. Addison-Wesley, Boston  
 Utterback N. G., Kissel J., 1990, *AJ*, 100, 1315  
 Veronig A., Temmer M., Hanslmeier A., Otruba W., Messerotti M., 2002, *A&A*, 382, 1070  
 Vigren E., Galand M., 2013, *ApJ*, 772, 33  
 Vigren E. et al., 2016, *AJ*, 152, 59  
 Woods T. N. et al., 2005, *J. Geophys. Res. (Space Phys.)*, 110, A01312  
 Zieba A., 2010, *Metrol. Meas. Syst.*, 17, 3

## APPENDIX : PROBE PHOTOEMISSION FROM ANALYSIS OF MULTIPLE SWEEPS, SUPPLEMENTARY MATERIAL

We investigate the accuracy of the multiple sweep analysis method with synthetic data for a range of plasma parameters. To model the total current, we use equations (1), (3) and (5). While in reality the noise level of the instrument is  $\pm 0.5$  nA, we do not add noise to our modelled current since we focus on the ideal limits of this method. The current response is modelled for  $V_S = -10$  V,  $V_b \in [-30, 30]$  V, fixed electron temperature at  $T_e = 5$  eV and varying ion velocity  $u$  and plasma density  $n$ . The slope of  $I_{\text{tot}}$  is then found by fitting a linear function to the synthetic current for  $V_p \in [-40, -30]$  V and  $I_{\text{tot}}$  is taken in the middle of that range from the fitted function, i.e.  $I_{\text{tot}}(V_p = -35\text{V})$ . In Fig. 5, we show results from the synthetic data for three different ion velocities,  $u = 0.1, 50$  and  $350$  km s $^{-1}$ . The solid lines are calculated with equation (7) for  $I_{\text{tot}} \in [-50, 0]$  nA for given ion velocity  $u$ . The important difference between the data points found from synthetic data and equation (7) is that the

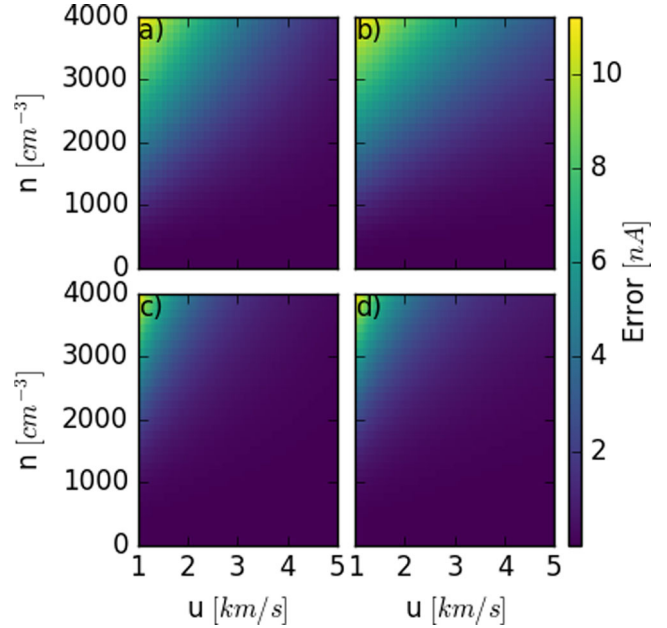


**Figure A1.** The error in  $I_{\text{ph0}}$  for two different levels of velocity variation  $\Delta u$  and two different ranges of  $V_p$ .  $V_p$  is varied for each column so that panels (a) and (c) have  $V_p \in [-40, -30]$  V. Panels (b) and (d) have  $V_p \in [-40, -25]$  V. Panels (a) and (b) have a velocity variation of  $\Delta u \simeq 117$  m s $^{-1}$  between the sweeps used for each grid square and for panels (c) and (d)  $\Delta u \simeq 38$  m s $^{-1}$ .

synthetic data includes an electron current. The increasing values of  $dI_{\text{tot}}/dV_p$  and  $I_{\text{tot}}$  for the data points correspond to increasing plasma density. One can see from the difference between the solid lines and the data points in Fig. 5 that the electron contribution becomes increasingly important for higher plasma density. Consequently, the slope can be overestimated due to the electron current. In the case of Fig. 5, extrapolating data with a single  $k$  would yield a large error in estimating  $I_{\text{ph0}}$ . In reality, the ion velocities would not change from  $0.1$  km s $^{-1}$  to  $350$  km s $^{-1}$  within a few sweeps.

To simulate more realistic plasma variations around comet 67P from sweep to sweep, we model the total current to the probe for a range of different parameters observed by RPCLAP. As can be seen from equations (7), and (3), the relevant plasma parameters are the plasma density and the ion energy. Since  $I_e$  is exponentially decreasing for  $V_p < 0$  it is expected that some contributions from  $I_e$  will affect our results, depending on the range of  $V_p$  we fit a linear function to. If the fitting range is not sufficiently below 0, the electron current might not be negligible. Hence, to investigate the error source attributed to electron currents, we change the range of  $V_p$  to which the linear function is fitted to against the synthetic  $I_{\text{tot}}$ . Furthermore, from equation (7), it is expected that with smaller ion velocity variations  $\Delta u$  between the sweeps this method is more accurate, and thus, we will also consider different  $\Delta u$  in the analysis.

We take the plasma density in the range of  $n \in [0, 4000]$  cm $^{-3}$ , the ion velocity in the range of  $u \in [1, 5]$  km s $^{-1}$ , and the electron temperature to be constant at  $T_e = 5$  eV. The range of  $n$  is subdivided into 35 equispaced intervals, while  $u$  is subdivided into two different equispaced intervals – with 35, and 105 intervals. Hence,  $\Delta n \simeq 117$  cm $^{-3}$  is constant, and  $\Delta u \simeq 117$  and  $38$  m s $^{-1}$ , respectively between the sweeps. Thus, creating two different grids with the size of  $35 \times 35$  and  $35 \times 105$ . Within each grid square nine different  $I_{\text{tot}}$  are created – one for each combination of  $n$  and  $u$ . For each  $I_{\text{tot}}$ , two different linear fits are fitted to the data – one fit for each  $V_p$ -range.

The  $I_{\text{ph0}}$  data set from the multiple sweep method is made possible due to a dynamic fitting routine of  $V_S$  (as previously mentioned in Section 2.3) such that the  $V_p$  range to estimate the slope and offset is also dynamic for each sweep, with most of the data set having  $V_p$  ranges between 10 and 15 V, and is also the chosen  $\Delta V_p$ -ranges in the synthetic sweeps. The slope  $dI_{\text{tot}}/dV_p$  is found from the fitted linear function, and  $I_{\text{tot}}$  is found in the middle of the  $V_p$ -range from the same fitted function.  $dI_{\text{tot}}/dV_p$  versus  $I_{\text{tot}}$  is then plotted, and a linear function is fitted these data points to extract  $I_{\text{ph0}}$ , as illustrated in Fig. 5.

In Fig. A1, we plot the error of  $I_{\text{ph0}}$  found by this method as compared to the  $I_{\text{ph0}} = -10$  nA we used to create the synthetic data. Panels (a) and (c) have a range of  $V_p \in [-40, -30]$  V, and panels (b) and (d) a range of  $V_p \in [-40, -25]$  V. We observe that this method remains accurate for lower plasma densities, even for a larger fitting range. The errors increase for increasing density, especially for fitting ranges closer to  $V_S$ , due to the exponential part

of the electron current. The error decreases for smaller ion velocity variations between the sweeps, i.e. with smaller  $\Delta u$ , as is illustrated by the difference between panels (b) and (d) of Fig. A1.

It is evident from Fig. A1 that this method is robust for most of the plasma conditions around 67P. A smaller range of  $V_p$  would reduce noise in the method, although instrumental noise provides a lower bound of the range of  $V_p$  for a good fit to be found. Further errors might be introduced due to heavy fluctuations of the ion energy in a very dense plasma. As previously mentioned, we do not expect this method to be sensitive to  $I_{\text{SEEP}}$ . If anything it would mitigate the electron retardation current influence on our  $I_{\text{ph0}}$  estimate, which we consider is our largest error source, due to the opposite sign and slope of the secondary electron current.

This paper has been typeset from a  $\text{\TeX}/\text{\LaTeX}$  file prepared by the author.

## Appendix B

### Paper II



# SIMULATIONS OF THE ROSETTA SPACECRAFT INTERACTION WITH COMET PLASMA

F. L. Johansson<sup>1,2,4</sup>, P. Henri<sup>1</sup>, A. Eriksson<sup>2</sup>, X. Vallières<sup>1</sup>, J-P Lebreton<sup>1</sup>, C. Béghin<sup>1</sup>, G. Wattieaux<sup>3</sup>, and E. Odelstad<sup>2,4</sup>

<sup>1</sup>Laboratoire de Physique et Chimie de l'Environnement et de l'Espace, CNRS, Orléans, France

<sup>2</sup>Swedish Institute of Space Physics, Uppsala, Sweden

<sup>3</sup>University Paul Sabatier Toulouse III in Toulouse, France

<sup>4</sup>Department of Physics and Astronomy, Uppsala University, Box 516, SE-75120 Uppsala, Sweden

## ABSTRACT

ESA's comet-chaser Rosetta is monitoring the plasma environment of comet 67P/CG since Summer 2014. Measurements from the Langmuir probes of the Rosetta Plasma Consortium have shown that the spacecraft often reaches negative potentials of around and in excess of -10 V, which affect in situ measurement of the plasma environment surrounding the spacecraft. To investigate the influence of spacecraft-plasma interaction on measurements of a cometary plasma, a series of SPIS simulations were carried out to investigate the spacecraft-plasma interaction and profile of the immediate plasma environment around Rosetta in the comet coma. We show the resulting electrostatic potential profile, as well as electron and ion densities in the vicinity of the Rosetta spacecraft, especially around the Mutual Impedance Probe and the Langmuir probes, with a spacecraft potential often reaching negative potentials of down to -20 V at different distances to the Sun and the comet. To help our understanding of in situ measurements of the plasma environment, we characterise the plasma inhomogeneities for the different operational modes on the Mutual Impedance Probe and in vicinity of the Langmuir probes.

Key words: Spacecraft-plasma interaction – Rosetta – comet– ESA – spacecraft potential – plasma density – Langmuir Probe – RPC-LAP – RPC-MIP.

## 1. INTRODUCTION

The comet-chaser Rosetta is monitoring the plasma environment of comet 67P/Churyumov-Gerasimenko (67P) since Summer 2014. Among the efforts dedicated to understanding the composition and evolution of the comet is the *Rosetta Plasma Consortium* (RPC), including the *Rosetta dual Langmuir probe instrument* (LAP) and the *Mutual Impedance Probe experiment* (MIP) as well as other instruments[1]. During the approach to perihelion and back, the 67P plasma environment has evolved

through at least four orders of magnitude of density. We observe very large changes on short timescales of the Rosetta *spacecraft potential* ( $V_{SC}$ ) during the mission due to plasma variations [7, 4, 8], which will affect all plasma instruments on-board as electrons and ions are attracted or repelled towards the spacecraft.

Previous simulations [3, 9] show that a proper interpretation of the plasma measurements on Rosetta need to take effects of the spacecraft potential into account. The extent of which we attempt to quantify and study in this report with further, more detailed simulations focused on a comet-like environment using *Spacecraft-Plasma Interaction System* (SPIS) [5].

We report here (1) on simulations of Rosetta spacecraft potential in a range of comet-like plasma environments, consistent with in situ measurements from Rosetta and (2) on the influence of such spacecraft potential on the plasma density surrounding Rosetta, were we find very inhomogeneous structures in need of further investigation.

## 2. INSTRUMENTS AND THEORY

Rosetta carries two instruments for characterizing the bulk plasma, the Langmuir Probe instrument LAP [2] and the Mutual Impedance Probe MIP [10]. More information on these can be found in the accompanying paper [4].

$V_{SC}$  is defined as the potential between the S/C and a plasma at infinity where the total current to the spacecraft is zero. A simple model for the current balance of a negatively charged spacecraft can be set up as follows. For supersonic ion flow, the ion current to a sphere is given by  $I_i = -qA_i n e u (1 - eV_{SC}/E_i)$ , where  $n$  is the plasma density,  $u$  is the flow speed,  $E_i = \frac{1}{2}m_i u^2$  is the energy of ions of mass  $m_i$ ,  $q$  is the charge, and  $A_i$  is the circular cross section [6]. The photoemission current is constant at its saturation value  $I_f = -A_f j_{f0}$ , where

$A_f$  is the cross-sectional area exposed to the sun. Neglecting secondary emission, the final component entering the current balance is the current due to plasma electrons,  $I_e = A_e j_{e0} \exp(eV_{SC}/k_B T_e)$ , where the thermal electron current density  $j_{e0} \propto n\sqrt{T_e}$ . Balancing these currents gives a transcendental equation for  $V_{SC}$ ,

$$A_i n e u \left(1 - \frac{eV_{SC}}{E_i}\right) + A_f j_{f0} = A_e j_{e0} e^{\left(\frac{eV_{SC}}{k_B T_e}\right)} \quad (1)$$

which can easily be solved numerically for  $V_{SC}$ . For the highly non-spherical Rosetta spacecraft, it is not obvious how  $A_i$  should be chosen, and when comparing to simulation results below we treat it as a free parameter, and rename numerical solutions for  $V_{SC}$  as  $V_{ref}$  for clarity.

### 3. SIMULATIONS

To investigate the expected spacecraft potential of Rosetta, SPIS simulations have been carried out for a range of cometary plasma parameters listed in Table 1. The simulation scenario was a quasi-neutral plasma with cometary ions of 19 amu of charge  $+e$ ,  $k_B T_{ion} = 0.1$  eV,  $u = 1$  km/s from the +X+Z (nadir) direction and the sun in the +X direction. Photoelectrons and secondary electrons from electron impact are also simulated with  $k_B T_f = k_B T_{SEE} = 2$  eV, respectively. All populations are simulated using *Particle In Cell* (PIC) motion except the input (primary) plasma electrons which are simulated using a Maxwell-Boltzmann fluid model approximation if and only if there are no attracting potentials in the volume.

### 4. RESULTS

In this section, we analyse the SPIS simulations of Rosetta's charging and discuss how it may affect the in situ measurements of MIP and LAP experiments.

#### 4.1. $V_{SC}$ behaviour in comet-like plasma

Grouping 12 simulations with identical plasma populations with varying distance to the sun, Figure 1 shows that the  $V_{SC}$  is driven to more negative potentials with increasing sun distance as the contribution of the photoelectron decreases with the solar flux. Comparing the four groups of simulations, we clearly see that increasing the electron temperature or the plasma density increases the electron current to the S/C and also drives the S/C more negative. This is generally in good agreement with Equation 1, as seen in Table 1, although the numerical solution is outside the limits of validity for positive spacecraft, and does not account for secondary electrons.

Table 1. Table of the simulation environment parameters,  $V_{SC}$  results from SPIS simulations and numerical results from Equation 1 denoted  $V_{ref}$

#	$d_{\odot}$ [AU]	$T_e$ [eV]	$n$ [ $cm^{-3}$ ]	$\lambda_d$ [m]	$V_{SC}$ [V]	$V_{ref}$ [V]
1	1.24	1	4000	0.1	-2.3	-2.0
2	1.24	1	1000	0.2	-1.1	-1.0
3	1.24	1	250	0.5	-0.4	0.3
4	1.24	1	100	0.7	1.9	1.2
5	1.24	5	4000	0.3	-14.7	-9.2
6	1.24	5	1000	0.5	-8.0	-7.1
7	1.24	5	250	1.1	-1.7	-2.3
8	1.24	5	100	1.7	1.5	1.9
9	1.24	10	100	2.3	-1.1	1.2
10	2	1	100	0.7	-1.3	0.3
11	2	5	250	1.1	-7.4	-5.9
12	2	5	100	1.7	-0.5	-2.5
13	2	10	100	2.3	-6.4	-7.4
14	3	1	100	0.7	-1.6	-0.5
15	3	5	250	1.1	-11.0	-7.9
16	3	5	100	1.7	-2.9	-5.6
17	3	10	100	2.3	-11.5	-12.2

#### 4.2. MIP LDL mode

MIP operates two different modes, namely the *LDL* and *SDL*, characterized by the use of different transmitters[10]. Indeed, the MIP spectra is flat, as expected in vacuum, if the emitter-receiver distance is shorter than the Debye length. In *SDL*, the MIP transmitters, located at 40 and 60 cm from the receivers, are used; while in *LDL* the LAP2 probe, located at 4 m from the receivers, is used as a transmitter, to operate in plasma characterized by a Debye length too large to be detected in *SDL*.

We hereafter focus on the *LDL* mode. As a signal is propagated from LAP2 to MIP receivers, a crude approach to investigate the effect of  $V_{SC}$  on MIP measurements is to visualise the density along the line of sight between the transmitter and receiver. The propagation of the MIP signal is beyond the scope of SPIS simulations, and not well understood for such an inhomogeneous plasma encountered around the Rosetta spacecraft. Therefore, considering a direct path from the emitter to the receiver is an approximation to be considered as a first step toward the understanding of the effect of spacecraft charging on MIP-*LDL* measurements.

The density structure around Rosetta resulting from spacecraft charging is shown in Figure 2 (from simulation in Table 1), with substantial electron density depletion around a -14.7 V spacecraft. Along the line of sight den-

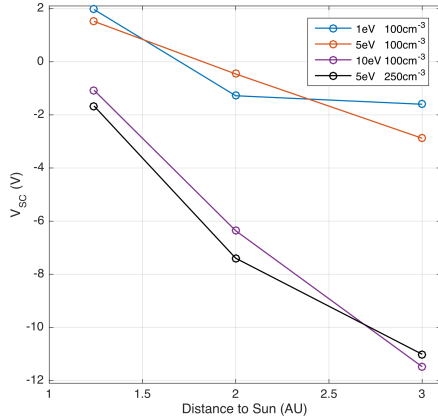


Figure 1.  $V_{SC}$  vs distance to the Sun plotted for four different plasma configurations of different electron temperature and plasma density, for a total of 12 simulations. Spacecraft potential decreases with increasing distance to sun, increasing plasma density and increasing electron temperature as the electron current becomes more dominant.

sity profile between LAP2 and MIP (not modelled), the density increases by a factor of 3 in  $\tilde{10}$  cm, and then stays moderately stable at  $1000 \text{ cm}^{-3}$ , a factor of 4 from the cometary electron density input into the simulation.

### 4.3. MIP SDL mode

In a separate simulation of only the spacecraft boom and the MIP instrument at floating potential, we see the detailed density profile close to MIP in a typical comet environment with the same parameters as simulation 7 in Table 1. Shown in the right plot of Figure 3, we see the electron depletion effect of a  $-5.5 \text{ V}$  spacecraft boom on the electron density profile around the MIP transceivers, on scales much smaller than the local Debye length, with a maximum line of sight negative charge) density in between the transceivers. Also a general trend of increasing of density closest to the end of the boom can be seen to the left in the plot. At both spacecraft and instrument scales, the simulations confirm the existence of local electron density inhomogeneities that may need to be taken into account in the MIP data analysis.

### 4.4. LAP

Visible both in the 3D density contour plots in Figure 2 and in the line profile density along the instrument field of view, we see clearly how the spacecraft potential deflects electrons when negative, resulting in a reduced plasma density in the immediate proximity of the probe. In the bottom plot of Figure 2, at a later stage in the same simulation, where LAP1 and LAP2 have a bias potential of  $+30 \text{ V}$  and  $0 \text{ V}$ , respectively from  $V_{SC}$ , we see

a density increase in the immediate proximity of LAP1 to about  $1000 \text{ cm}^{-3}$ , a quarter of the input density, at the probe position. This decreases radially as the electrostatic potential profile decreases from  $+15.3 \text{ V}$  to  $0$  within  $10 \text{ cm}$  and is completely enveloped by the potential field of the spacecraft within  $20 \text{ cm}$ . A bias potential sweep to  $+30 \text{ V}$  will therefore possibly not enable LAP to sample a volume with an unperturbed electron density when the spacecraft is highly charged.

## 5. CONCLUSIONS

In this parametric study, we study the influence of the comet evolution on the spacecraft-plasma induced environment, as we escort the comet to and from perihelion, for a number of cases relevant for both observed comet activity and distance to the comet[4]. The result can be used both to predict effects on MIP and LAP measurements, as well as be exported for further instrument specific studies e.g. dust and particle trajectories, and simulations of the propagation of the MIP signal.

We observe an expected spacecraft potential evolution as a function of solar UV flux, i.e. S/C photoemission current, electron temperature and plasma density in agreement with analytic results, as well as predict density depletion around the spacecraft, which may affect LAP and MIP measurements. For further investigation of instrument performances, the authors strongly suggest simulating a Langmuir Probe sweep within the simulation, and a more quantitative approach to the effect of local plasma inhomogeneities on the MIP measurements.

## ACKNOWLEDGMENTS

Rosetta is a European Space Agency (ESA) mission with contributions from its member states and the National Aeronautics and Space Administration (NASA). The work on RPC-LAP data was funded by the Swedish National Space Board under contracts 109/12, 135/13, and 166/14 and Vetenskapsrådet under contract 621-2013-4191. Work at LPC2E/CNRS was supported by CNES and by ANR under the financial agreement ANR-15-CE31-0009-01. The authors benefitted from the use of the cluster at the Centre de Calcul Scientifique en région Centre-Val de Loire (CCSC).

## REFERENCES

- [1] Carr, C., Cupido, E., Lee, C. G. Y., et al. 2007, Space Sci. Rev.
- [2] Eriksson, A. I., Boström, R., Gill, R., et al. 2007, Space Sci. Rev., 128, 729
- [3] Eriksson, A. I., Hånberg, C., & Sjögren, A. 2010

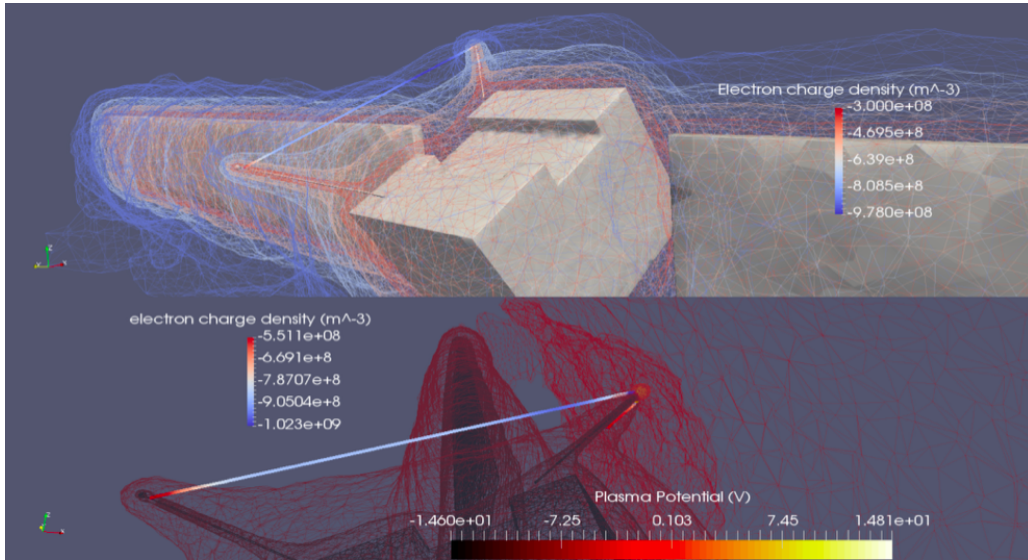


Figure 2. Top: Plasma electron density iso-surfaces (increasing density from blue to red), showing how a  $-14.6$  V negatively charged spacecraft model deflects electrons away from the spacecraft. Also pictured line of sight density map from LAPI to LAP 2, which is the baseline for LDL measurements. Below: Equipotential shells (yellow to black) around a spacecraft model with a  $+15.4$  V charged LAPI probe. Also pictured: line of sight density map (increasing density from blue to red) for LDL and SDL (parallel to LAPI boom).

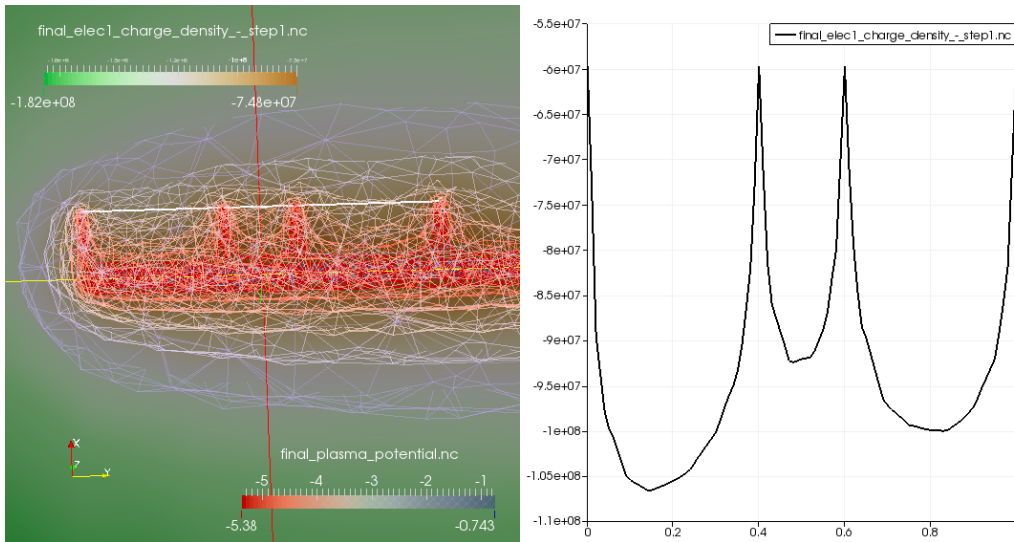


Figure 3. Equipotential shells (blue to red) and density profile (brown to green) around MIP, a simulation of a LAPI boom and 4 MIP probes in plasma parameters similar to Simulation 7 in Table 1. The whole structure is electronically connected, conducting and converged to a potential of  $-5.38$  V. Left: Electronic charge density distribution ( $\text{cm}^{-3}$ ) cut along X-Y plane at  $Z = 0$  from green to brown and plasma potential equipotential shells from red to blue. The white line is the line of sight plotted to the right. Right: Line of sight charge density (negative) ( $\text{cm}^{-3}$ ) profile from the MIP transmitter furthest from the spacecraft at 0 to the fourth MIP probe closest to Rosetta at 1 m.

- [4] Eriksson et al., A. 2016, in Proceedings of the 14th Spacecraft Charging Technology Conference (European Space Agency), this issue
- [5] Matéo-Vélez, J.-C., Sarrailh, P., Thiébault, B., et al. 2012, 12th Spacecraft Charging Technology Conf. Kitakyushu, Japan
- [6] Medicus, G. 1961, Journal of Applied Physics, 32, 2512
- [7] Odelstad, E., Eriksson, A., Edberg, N., et al. 2015, in EGU General Assembly Conference Abstracts, Vol. 17, EGU General Assembly Conference Abstracts, 12379
- [8] Odelstad, E., Stenberg-Wieser, G., Wieser, M., et al. 2016, in Proceedings of the 14th Spacecraft Charging Technology Conference (Noordwijk, NL, April 4-8, 2016), Abstract 123, this issue.
- [9] Roussel, J.-F. & Berthelier, J.-J. 2004, Journal of Geophysical Research (Space Physics), 109, A01104
- [10] Trotignon, J. G., Michau, J. L., Lagoutte, D., et al. 2006, Space Science Reviews, 128, 713